

THESIS FOR THE DEGREE OF DOCTOR OF PHILOSOPHY

Construction of an Arbitrary Waveform Radar System

Martin Ankel



CHALMERS

Quantum Technology (QT)
Department of Microtechnology and Nanoscience (MC2)
CHALMERS UNIVERSITY OF TECHNOLOGY
Göteborg, Sweden 2024

Construction of an Arbitrary Waveform Radar System

Martin Ankel

ISBN 978-91-8103-081-5

Acknowledgments, dedications, and similar personal statements in this thesis reflect the author's views.

© MARTIN ANKEL, 2024.

Doktorsavhandlingar vid Chalmers Tekniska Högskola

Ny serie nr. 5539

ISSN 0346-718X

Quantum Technology (QT)

Department of Microtechnology and Nanoscience (MC2)

CHALMERS UNIVERSITY OF TECHNOLOGY

SE-412 96 Gothenburg

Telephone +46 (0)31 772 1000

Front Cover: A picture of the developed L-band transmitter unit mounted underneath a hovering unmanned aerial vehicle.

Printed by Chalmers Reproservice, Chalmers University of Technology
Göteborg, Sweden, 2024

Construction of an Arbitrary Waveform Radar System
Martin Ankel
Department of Microtechnology and Nanoscience (MC2)
Chalmers University of Technology

Abstract

The thesis aims to develop and deploy continuous wave noise radar systems by addressing the self-interference issue and considering real-time implementation aspects. In contrast to the traditional pulse-Doppler radar, which generally operates with short, high-powered, and deterministic pulses, noise radars transmit continuous, low-powered, random, and preferably wideband signals. Noise radar systems offer several advantages over pulse-Doppler systems. The most notable (and desired) advantage is their low probability of interception properties – detecting and localizing a noise radar system is more challenging than a pulse-Doppler radar system.

However, few (or none) commercial or military noise radar systems exist due to the challenge of achieving relevant performance. The main problem is that self-interference, such as direct signal interference or clutter echoes, severely restricts the system's detection sensitivity. A significant amount of research has been dedicated to resolving the self-interference problem, and although good results have been achieved, more is required. Noise radar signal processing also requires high-speed digital electronics, and it is only recently that the performance of digital electronics has started to be on par with the requirements.

In this thesis, bistatic noise radar is considered a solution to the self-interference problem. By constructing a bistatic noise radar system, it is shown that separating the transmitter and receiver reduces the self-interference, thereby increasing the detection sensitivity. Furthermore, bistatic operation enables adaptive beamforming, which can be applied to further suppress self-interference – this is demonstrated using a multichannel receiver.

A real-time processor operating with a time-bandwidth product of 77 dB is implemented on a state-of-the-art field programmable gate array to investigate limiting aspects of real-time noise radar systems. The processor demonstrates that wideband noise radar systems are possible, but several limiting factors exist. One limitation is that operating with high time bandwidth products leads to several effects, such as range-walk, Doppler spread, and target decoherence, which must be managed. These effects are shown using offline data, and solutions are successfully applied. However, implementing these solutions in real-time systems is still an open question.

The most significant outcome of the thesis is the construction of a real-time bistatic noise radar system capable of detecting small UAVs at an operationally relevant distance of over 3.2 km. Minor improvements can significantly increase the detection range. This achievement demonstrates the readiness of noise radar technology for commercial adoption, reinforcing the thesis's primary goal.

Keywords: Noise Radar, Bistatic Radar, Continuous Wave Radar, Real-Time Radar, Digital Beamforming, Range Walk, Low Probability of Intercept Radar, Air Surveillance Radar, Clutter Filter, Correlation Noise Floor

Publications Included in the Thesis

I Bistatic Noise Radar: Demonstration of Correlation Noise Suppression

M. Ankel, R. Jonsson, T. Bryllert, L. M. H. Ulander, and P. Delsing
IET Radar Sonar & Navigation, vol. 17, pp. 351-361, 2023

II Experimental Evaluation of Moving Target Compensation in High Time-Bandwidth Noise Radar

M. Ankel, R. Jonsson, M. Tholén, T. Bryllert, L. M. H. Ulander, and P. Delsing
20th European Radar Conference (EuRAD), pp. 213-216, 2023

III Implementation of a Coherent Real-Time Noise Radar System

M. Ankel, M. Tholén, T. Bryllert, L. M. H. Ulander, and P. Delsing
IET Radar Sonar & Navigation, vol. 18, pp. 1002–1013, 2024

IV Real-Time Bistatic Noise Radar with Adaptive Beamforming

M. Ankel, R. Jonsson, M. Tholén, T. Bryllert, L. M. H. Ulander, and P. Delsing
2024 IEEE International Radar Conference (RADAR), 2024
Accepted for publication

V Aspects of Operating Low-Cost Bistatic Radar Transmitters

M. Ankel, T. Bryllert and J. Backlund
2024 IEEE International Radar Conference (RADAR), 2024
Accepted for publication

Other Publications

VI Experimental Analysis of a Clutter Suppression Algorithm for High Time-Bandwidth Noise Radar

R. Jonsson, **M. Ankel**, M. Tholén, T. Bryllert, L. M. H. Ulander, P. Delsing, and P. Dammett
2023 IEEE International Radar Conference (RADAR), pp. 1-6, 2023

VII A Comparison Between Quantum and Classical Noise Radar Sources

R. Jonsson, R. D. Candia, **M. Ankel**, A. Ström, G. Johansson
2020 IEEE Radar Conference (RadarConf20), pp. 1-6, 2020

VIII Quantum Radar – What is it Good For?

R. Jonsson and **M. Ankel**
2021 IEEE Radar Conference (RadarConf21), pp. 1-6, 2021

Acknowledgements

The results accomplished in this thesis were only possible thanks to the assistance and commitment of several people, to whom I am grateful. First, I would like to express my gratitude to my supervisor, Prof. Per Delsing, for your excellent mentorship. You always encouraged and inspired me and constantly provided insightful comments and valuable contributions, showing testament to your greatness as a researcher.

And thanks to my co-supervisors, Prof. Lars Ulander and Tomas Bryllert. Lars, I'm thankful for you coming aboard and taking the time to co-supervise when the project changed direction. Your vast expertise and experience in radar have been invaluable. Tomas, not only my supervisor but also my fellow Saab colleague, your broad knowledge of all aspects relating to radar systems, from specific details in PCB design to the broader view of system design and radar operation, has been truly inspiring. You always took the time to assist me when I needed it, and your mentorship has had a profound impact in shaping me into the radar engineer I am today. Having you as a supervisor and a colleague has been an absolute pleasure, and I look forward to continuing working with you on the many exciting projects ahead.

Thank you, Robert Jonsson and Mats Tholén, for being the best collaborators one could have. Robert, your extensive knowledge and skill in signal processing are truly impressive and have been vital to the project's success. Discussing and working with you has been my privilege; I learned a lot. You have been an amazing friend and colleague, and I look forward to continuing to work with you. Mats, you took me under your wing and mentored me in the fine art of FPGA programming, for which I am grateful. It is much thanks to you that the real-time system has become a reality. I wish you the best of luck in your future career.

I would also like to thank my colleagues at Saab and the Quantum Technology group at Chalmers. You have all created an inspiring and welcoming environment, allowing me to grow as a researcher and person. All the love to my family, and thank you for your never-ending support and encouragement.

Lastly, I would like to thank the KAW Foundation and Saab for giving me the opportunity to conduct my PhD thesis.

Acronyms

- ADC** Analog-to-Digital Converter
- BRAM** Block Random Access Memory
- CAF** Cross Ambiguity Function
- CFAR** Constant False-Alarm Rate
- CA-CFAR** Cell-Averaging Constant False-Alarm Rate
- CNF** Correlation Noise Floor
- CPI** Coherent Processing Interval
- CPU** Central Processing Unit
- CUT** Cell Under Test
- CW** Continuous Wave
- DAC** Digital-to-Analog Converter
- DRAM** Dynamic Random Access Memory
- DSP** Digital Signal Processing
- ECA** Extensive Cancellation Algorithm
- ENBW** Equivalent Noise Bandwidth
- ESM** Electronic Support Measures
- FFT** Fast Fourier Transform
- FIR** Finite Impulse Response
- FPGA** Field-Programmable Gate Array
- GNSS** Global Navigation Satellite System
- GPU** Graphics Processing Units
- HDL** Hardware Description Language
- HPA** High Power Amplifier
- LFSR** Linear Feedback Shift Registers
- LIPO** Lithium-Ion Polymer
- LPE** Low Probability of Exploitation
- LPI** Low Probability of Intercept

LPID Low Probability of Identification
MIMO Multiple-Input and Mutiple-Output
NRT Noise Radar Technology
PAPR Peak-to-Average Power Ratio
PASR Peak-to-Average Sidelobe Ratio
PCB Printed Circuit Board
PPS Pulse Per Second
PRF Pulse Repetition Frequency
PRI Pulse Repetition Interval
PSD Power Spectral Density
RADAR RAdio Detection And Ranging
RCS Radar Cross Section
RF Radio Frequency
RS Recommended Standard
SDR Software-Defined Radio
SINR Signal-to-Interference-Plus-Noise Ratio
SNR Signal-to-Noise Ratio
TRL Technology Readiness Level
TTD True Time Delay
UAV Unmanned Aerial Vehicle
USB Universal Serial Bus
VNA Vector Network Analyzer
WACQT Wallenberg Center for Quantum Technology

List of Symbols

Symbol definitions might differ from the appended papers.

a	Fractional time delay
b	Number of bits of each LFSR sample
B	Waveform bandwidth
c	Speed of light in vacuum
dr	Range resolution
dv	Velocity resolution
df	Frequency resolution
d	Antenna diameter
D	Dowsampling parameter
e_n	Time window coefficients
f_s	Baseband sampling rate
f_r	DAC/ADC sampling rate
f_c	Carrier frequency
f_D	Doppler shift
F	Noise figure
g	Antenna shape constant
G_T	Transmitter gain
G_R	Receiver gain
h_n	FIR-filter taps
J	Number of Doppler cells suppressed in the clutter suppression
k	Discrete propagation delay
k_B	Boltzmann's constant
K	Partial correlation coefficient
K_R	Number of range-walk cells
K_D	Number of Doppler spread cells
l	LFSR filter polynomial degree
L	General loss term
L_D	Doppler loss
L_S	Range-walk and Doppler spread loss
L_{corr}	Correlation loss
M	Number of samples in a pulse or batch
N	Number of waveform samples
P	Number of pulses or batches
P_T	Peak power
R	Range to target
R_{\max}	Maximum detection range
R_a	Unambiguous detection range
S	Number of antenna elements
t_{rep}	LFSR repetition time
t_{rt}	Round trip time of the signal
t_p	Length of the time domain window
T_0	Reference temperature
T_{int}	Integration time

T_{\max}	Maximum integration time
v	The target's velocity
v_{ra}	The target's radial velocity
v_r	Velocity hypothesis
v_j	Clutter velocity
\vec{v}	Target velocity vector
v_a	Unambiguous velocity
V	Number of velocity hypotheses
V_D	Drain voltage
V_G	Gate voltage
w_n	Antenna element weights
$x(t)$	Complex baseband representation of the reference signal
$x(t)_{re}$	Real value of $x(t)$
x^f	Forward projection error of the lattice filter
x^b	Backward projection error of the lattice filter
x_n	Discrete reference signal
\vec{x}	Reference signal vector
X	Fourier transformed reference signal
$y(t)$	Complex baseband representation of the received signal
$y(t)_{re}$	Real value of $y(t)$
y_n	Discrete received signal
\vec{y}	Received signal vector
Y	Fourier transformed received signal
α	Target amplitude
β	Clutter amplitude
δ	Duty cycle
Δv	Velocity hypothesis spacing
η	Radar cross section
θ	Angle between radar boresight and the target velocity vector
θ_{3dB}	Antenna 3 dB beamwidth
θ_{acc}	Angular accuracy
κ	Detection threshold
λ	Wavelength
Λ	Resolution cell
μ	Pulse length or batch length
ν_n	Internal receiver noise
ρ_k	Discrete cross-correlation
$\vec{\rho}$	Vector cross-correlation
σ	Signal variance
σ_S	Auto-correlation variance
τ	Farrow filter target delay
$\hat{\tau}$	Farrow filter actual delay
τ_Φ	Phase delay
X	Cross ambiguity function
ϕ	Direction of the main lobe
Φ	Phase shift

Contents

1	Introduction	1
1.1	Noise Radar History	3
1.2	Quantum Radar	4
1.3	Passive Radar	5
1.4	Thesis Background and Aim	5
1.5	Structure of the Thesis	6
2	Theory	7
2.1	Pulse-Doppler Radar	7
2.1.1	Range Measurement and Range Resolution	7
2.1.2	Velocity Measurement and Velocity Resolution	9
2.1.3	Range and Velocity Processing Summarized	10
2.1.4	Detector – Constant False Alarm Rate	11
2.1.5	Angular Resolution and Accuracy	12
2.1.6	Radar Range Equation	12
2.1.7	Bistatic Radar	13
2.2	Noise Radar	14
2.2.1	Waveform Generation – Linear Feedback Shift Registers . . .	14
2.2.2	Cross Ambiguity Function	15
2.2.3	Correlation Noise Floor – Masking Effect	18
2.2.4	Efficient Range-Doppler Processing – Batched Processing .	19
2.2.5	Doppler Tolerance	21
2.2.6	Range-Walk and Doppler Spread	22
2.2.7	Clutter Suppression – CLEAN and Lattice Filter	24
2.3	Beamforming	25
3	Hardware and Firmware Development	29
3.1	Bistatic Transmitter	30
3.1.1	Waveform Generation Plane	32
3.1.2	Control Plane	32
3.1.3	Power Amplification Plane	34
3.2	Vivace – Real-Time Noise Radar	35

3.2.1	Offline Data Collection	37
3.2.2	Matlab User Interface	38
3.2.3	FPGA Resource Utilization	38
3.2.4	Calibration	38
4	Results	41
4.1	CLEAN and Lattice Filter	41
4.2	Adaptive Beamforming	43
4.3	Paper Summaries and Main Findings	43
5	Conclusions and Outlook	49
	Bibliography	51
	Appended Paper I	61
	Appended Paper II	75
	Appended Paper III	81
	Appended Paper IV	95
	Appended Paper V	103

Chapter 1

Introduction

Noise radar technology (NRT) refers to the use of noise-like waveforms in radar systems to perform coherent detection. In 1959, B.M Horton recognized that range ambiguities could be mitigated by transmitting random noise and cross-correlating the received echo with a delayed copy of the transmitted signal [1, 2]. A simplified block diagram of an early adaptation of such a system is shown in Fig. 1.1. Noise is generated and filtered to an appropriate bandwidth; part of the signal is transmitted, and the other part is delayed and used for cross-correlation with the received echo. A mixer and a lowpass filter perform the cross-correlation. If the time delay matches the round-trip time of the transmitted signal, the mixer output voltage is low and a detection is declared. Thanks to the random, or specifically, non-repeating nature of the noise waveform, detection is only declared if the round trip time matches the time delay. Therefore, the system does not suffer from range ambiguities.

Horton originally intended the proposed system to function as an altimeter in a blind landing system, in which erroneous range measurements could result in disaster. However, the primary motivation behind past and present noise radar research is the expectation that high bandwidth, low peak power, and random waveforms will provide low probability of intercept (LPI) properties [3–6]. LPI means that the radar operates so that the emitted signal is not easily detected by electronic support measures (ESM) systems; the radar can be considered silent. To keep the transmitted power low, noise radars generally transmit continuously and integrate the received signal for an extended time to maintain adequate detection ranges. The reason behind operating with high bandwidth and low power is to distribute the transmitted energy in time and frequency, aiming to achieve a power spectral density (PSD) lower than the thermal PSD of the ESM receiver – thereby forcing the ESM system to perform incoherent integration. Still, the radar has a massive disadvantage in terms of two-way propagation compared to the ESM system’s one-way propagation, and for the radar to overcome this disadvantage, the time-bandwidth product must be high. Operating with high time-bandwidth products is difficult – as will be demonstrated – and the question is whether noise radars offer any LPI properties if given reasonable assumptions [7–9].

However, introducing randomness to the waveform has other advantages. Even

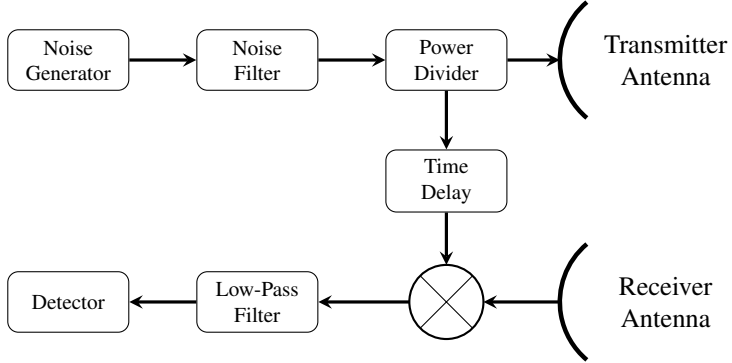


Figure 1.1: Noise Radar Block Diagram This is a block diagram of an early adaptation of an analog noise radar system [1, 2]. Noise is generated and filtered to an appropriate bandwidth. One part of the noise signal is transmitted, and the other is time-delayed. If the time delay matches the round-trip time of the transmitted signal, the mixer output is low – specifically, the mixer calculates the anti-correlation. A lowpass filter removes higher-order mixer products before passing the resulting signal to the detector.

if the radar transmission is detected, limited information is revealed, and classifying the radar system will be challenging. For example, the radar mode of operation is difficult to deduce since the waveform does not have a pulse repetition frequency (PRF). Therefore, noise radars are said to operate with a low probability of exploitation (LPE) [10] and a low probability of identification (LPID) [5]. Another advantage is that the orthogonality between different noise waveforms naturally results in low mutual interference [11, 12], allowing several systems to operate simultaneously within the same frequency band.

Additionally, noise radars are free from range ambiguities, as mentioned above, and they are also free from Doppler ambiguities [6, 13–16]. However, one of the more exciting aspects of noise radar development, in the author’s opinion, is the possibility of operating continuous and arbitrary waveforms. A broadband noise radar system can operate with any waveform without requiring signal processing or system architecture changes. The radar could, for example, transmit telecommunications signals to disguise itself or to improve spectrum compatibility.

Unfortunately, noise radars also have many disadvantages, severely hindering their implementation. The most limiting drawback with noise radars is that the auto-correlation of the waveform produces a uniform noise floor, referred to as the correlation noise floor (CNF) – also commonly known as the *masking effect* [4, 17, 18]. The limitations in detection sensitivity imposed by the CNF are illustrated in Fig. 1.2. The weaker echo from the airplane is disguised by the CNF originating from the stronger echo of the mountain. Often, the CNF limits the detection sensitivity of noise radar systems to a few hundred meters. The CNF is detailed in Section 2.2.3.

In appended paper IV, we are the first, to the authors’ knowledge, to demonstrate a broadband and real-time noise radar surveillance system not limited by the CNF. The constructed system operates in a bistatic mode and can detect small unmanned aerial

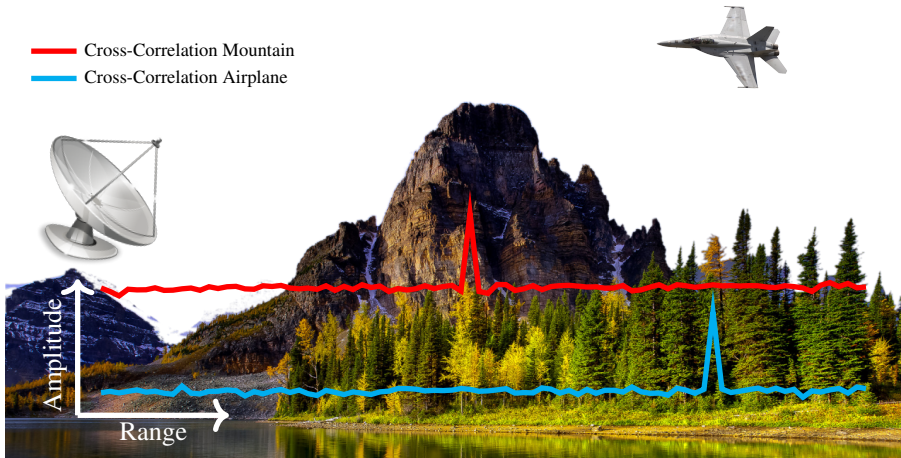


Figure 1.2: Correlation Noise Floor Illustration This illustrates how the correlation noise floor (CNF) limits the detection sensitivity in noise radars. The mountain’s correlation sidelobes disguise the airplane’s main peak, resulting in the target of interest, the airplane, being undetected.

vehicles (UAVs) at a range of more than 3.2 km. The detection range is only limited by output power and antenna gain. A more powerful transmitter will significantly increase the detection range. It is a significant milestone, but much work is still required before noise radars are mature enough for widespread implementation.

1.1 Noise Radar History

Although B.M Horton’s publication in 1959 is generally considered the starting point of noise radar research, the use of noise signals in radar dates back to 1897 when Alexander S. Popov used noise pulses in his telecommunications experiments [19]. He noticed that a ship passing through the electromagnetic signal path resulted in a detectable disturbance, demonstrating the first bistatic radar. The idea was later patented by Christian Hülsmeier in 1904 [20]. He called his invention the *Telemobiloskop*. Both C. Hülsmeier and A. Popov used noise pulses generated by a spark generator. However, neither A. Popov’s observation nor C. Hülsmeier’s invention prompted any development until the 1930s. During the 1930s, eight countries independently developed radar systems, such as Great Britain’s notable chain home system. The Second World War signified the importance of radar surveillance, leading to a significant surge in radar development and ushering in a new area of military radar [21].

The origins of coherent noise radars date back to the late 1950s. In 1957, R. Bourett proposed the first range-measuring radar system based on noise waveforms [22]. The proposed design utilized a double differentiation circuit between the delay line and the correlator. However, concerns were raised that his design was not practically realizable [23,24]. Horton solved the issue by instead proposing the more practical

cross-correlation method shown in Fig. 1.1. Horton's work has formed the basis of developed noise radar systems ever since.

Noise radar research continued in the 1960s and 1970s by a handful of researchers [2, 25–31]. Besides the masking effect, there were also limitations in the available hardware at the time. These early systems were analog, thus requiring analog microwave delay lines to calculate the cross-correlation. Considering that an analog system requires one analog delay line per range cell, a system with reasonable range resolution and coverage was too complicated of an engineering challenge. Especially as even today, there are no low-loss analog microwave delay lines.

In 1978, it was proposed to perform the cross-correlation in the digital domain [31] where multiple range cells can be processed in parallel. Digital processing, however, demands high-speed electronics, which was not available at the time. It was not until the mid 1990s that further progress was made. Since then, a significant amount of work has been carried out in both theoretical advancements [1, 5–8, 12–14, 16, 32–36] and practical work [9, 18, 32, 37–51].

However, even today the fundamental problem of the masking effect remains. The 2010s can be considered as the time when much effort was focused on clutter suppression, which means eliminating signals originating from clutter. Clutter refers to all signal returns that are of no interest. Conventional clutter suppression methods, often used in pulsed systems, for example, moving target indicator and moving target detection filters [52, 53], have no effect on the CNF. Instead, other methods are required [17, 54–63]. A drawback of clutter suppression algorithms is the computational cost. Additionally, the performance is generally not good enough to, on its own, solve the masking effect issue.

In the later years, the focus has shifted towards waveform shaping [6, 47, 49, 64–66] – modifying the noise waveform to have lower correlation sidelobes. Many groups now consider well-isolated receiving and transmitter antennas and shaped waveforms as their system solution. However, isolating the receiving and transmitter antennas is not necessarily a scalable solution and does not protect against close-range ground clutter.

1.2 Quantum Radar

In 2009, S. Lloyd published a paper about *Quantum Illumination* [67], which seems some radar engineers took notice of and thought: "This looks like a noise radar, only quantum." That realization spurred the field of *Quantum Radar*, also referred to as *Quantum Noise Radar* due to the similarities to the classical noise radar. The general idea behind quantum radar is to create entangled photon pairs. One photon is transmitted, whereas the other is retained and used to perform cross-correlation. Quantum theory tells us that the correlation between two entangled photons is stronger than that for two classical photons; an often-cited improvement figure in the quantum radar papers is 6 dB [68]. The problem with quantum radar is that none of the advantages remains after amplification to relevant output powers, and constructing a working system is not possible due to a lack of technology. For more information about quantum radars and their limitations, see papers VII and VIII and references [69–71].

1.3 Passive Radar

Another field very similar to noise radar is passive radar [72–78]. Passive radar systems suffer from many of the same problems as noise radars, and similar solutions are applied in both fields. The major drawback of passive radar systems is the reliance on illuminators of opportunity, which does not necessarily guarantee a quality of service. However, since much is similar, there are things to learn from the passive radar community and vice versa. The passive radar community has also performed several impressive demonstrations; for example see references [59, 79–82].

1.4 Thesis Background and Aim

The thesis was a joint project between Saab and Chalmers within the Wallenberg Center for Quantum Technology (WACQT) research program. The original aim was to investigate the idea of quantum radar and determine its applicability to future radar systems. After a preliminary investigation, it was concluded that quantum radar is currently not of practical interest – see paper VII and paper VIII. Instead, the parties involved agreed to explore noise radars, specifically radars operating with continuous arbitrary waveforms. Rather than following in the footsteps of other groups – mainly focusing on algorithm development – the idea was to take a more system-oriented approach and construct a real-time demonstrator. The goal was that demonstrator should operate with high time-bandwidth products and detect UAVs at several kilometers. Additionally, the detection sensitivity should not be limited by the CNF.

It was decided that operating bistatic continuous wave transmitters and having digital monostatic radars acting as receivers were the preferred systems approach. Not only is the clutter, and thereby the CNF, naturally reduced in a bistatic configuration, but bistatic operation is also beneficial from a system architecture view. It is doubtful that noise radars will replace traditional radars. However, monostatic digital radars can operate as receivers with bistatic noise transmitters without requiring hardware changes. Noise radar is then only one mode of operation among many. If the cost of the transmitter is low, relative to the receiver – which the author believes it is with proper design – the investment and, thereby, the risk of implementing noise radar systems is low, possibly expediting the process of bringing noise radars to market. Other advantages of bistatic noise radar are further discussed in the appended papers.

In the first paper, appended paper I, bistatic noise radar offline proof-of-concept experiments were performed, showing good results in suppressing the CNF. Much emphasis was placed on developing a highly capable and lightweight transmitter, whereas the receiver, in this case, was a simple one-channel software-defined radio (SDR). Additionally, two clutter cancellation algorithms were investigated, which led to the development of the Sequential CLEAN algorithm. Realizing that operating with high time-bandwidth products will result in target range-walk and Doppler spread (see Section 2.2.6), a real-time applicable method to compensate for this was required before developing a real-time noise radar processor. In appended paper I, the range-walk and Doppler spread problem was circumvented by flying the UAV very slowly.

Appended paper II investigated the performance of a moving target compensa-

tion algorithm to account for range-walk and Doppler spread. The moving target compensation algorithm is a known technique, but experimental results are lacking. The results showed excellent compensation of up to 20 dB improvement in signal-to-interference-plus-noise ratio (SINR), which aligned with theoretical predictions. Additionally, coherent integration times of a UAV were investigated and shown to be up to 2.5 s.

Based on the results above, the author was confident enough to implement a field-programmable gate array (FPGA) based digital real-time noise radar processor – the system is detailed in appended paper [III](#). The first version was a monostatic system; therefore, the CNF severely limited the detection performance. However, the demonstration proved that the real-time signal processing worked for time-bandwidth products of up to 77 dB and that the online moving target compensation was successful. A video of the demonstration is seen in reference [\[83\]](#).

Continued work improved the real-time system; see appended paper [IV](#). Besides implementing bistatic functionality, the receiver now utilizes eight receiving channels – as opposed to only one receiving channel as in appended paper [III](#) – allowing for adaptive beamforming to mitigate self-interference. In the paper, we demonstrate real-time detection of small UAVs at a range of 3.2 km and perform offline beamforming analysis to suppress self-interfering signals. Also, for this demonstration, a video is provided in reference [\[83\]](#).

The final paper, appended paper [V](#), illustrates the difficulties of operating with long integration times and high bandwidths and presents possible strategies to manage these difficulties. It is not a noise radar paper; experiments are performed with a traditional pulsed radar transmitter, but the difficulties remain the same. The paper is based on work the author carried out in service of Saab. Thus, some of the results and data are anonymized. The points made are, however, clearly illustrated. In short, managing high time-bandwidth products will be extremely difficult in practice, limiting the possibility of noise radars achieving LPI.

Paper [VI](#) is outside the scope of this thesis, but it considers clutter cancellation in noise radar systems and is highly relevant to the overall work. The paper's main objective was to implement a competent but computationally efficient clutter cancellation algorithm. By implementing a variant of the extensive cancellation algorithm (ECA), suppression of up to 30 dB was achieved. More information about the implementation is found in reference [\[71\]](#).

1.5 Structure of the Thesis

Chapter [2](#) presents the necessary theoretical framework, it describes the traditional pulse-Doppler radar, beamforming techniques, and the relevant noise radar concepts. In Chapter [3](#), the hardware and firmware developed are described, including the transmitter and the real-time processor. Chapter [4](#) provides additional results not present in the appended papers and summarizes each of the appended papers. Chapter [5](#) summarizes the thesis and presents future research directions.

Chapter 2

Theory

The purpose of this chapter is to provide the theoretical background required to understand the results presented. For deeper theoretical knowledge, the reader is advised to read references [35, 52, 53, 84].

The beginning of this chapter is devoted to radar fundamentals, where the commonly used pulse-Doppler radar is introduced. Pulse-Doppler radar is the premiered radar system for military use and is used as a reference when discussing the pros and cons of noise radar operation. Next, theoretical aspects relating to broadband noise radar operation are detailed. Lastly, the concept of beamforming is introduced.

2.1 Pulse-Doppler Radar

Radar are used for various sensing applications, both military and civilian. A typical application is surveillance, where the two essential functions are inherent in the word *RAdio Detection And Ranging* (RADAR). Other functions include determining the target's velocity and position. Additionally, some radars also perform tracking and, if possible, target identification.

This section describes the range and velocity processing basics in pulsed radar systems. It is followed by a description of a typical detector. Next, the angular resolution and accuracy of an antenna are defined. Then, the radar range equation is formalized. Lastly, the concept of bistatic radar is introduced.

2.1.1 Range Measurement and Range Resolution

The operation of a pulsed radar system is illustrated in Fig. 2.1. The radar transmits a series of high-powered electromagnetic pulses $x(t)$ of length μ and listens to the echo signals $y(t)$. In the thesis, $x(t)$ and $y(t)$ refers to the complex representation of the baseband signal. Often, transmitting while receiving saturates the receiver, so pulsed radars alternate between transmission and reception, resulting in blind zones. Blind zones correspond to the ranges where echoes return while the receiver is turned off.

To minimize the extent of blind zones, the pulse length μ is usually short, and the time spent receiving is long, leading to low duty cycle δ .

The range to target R is given by the round-trip time t_{rt} of the pulse times the speed of light c divided by two. Unfortunately, pulsed radar suffers from range ambiguities – uncertainty which of the transmitted pulses is received. The maximum unambiguous range R_a equals the pulse repetition interval (PRI) – the time between pulses – times c divided by two. Hence, the range to target is given by

$$R = \frac{t_{\text{rt}} \cdot c}{2} + R_a \cdot n = \frac{t_{\text{rt}} \cdot c}{2} + \frac{\text{PRI} \cdot c}{2} n, \quad n = 0, 1, 2, \dots, n_{\max}, \quad (2.1)$$

where for $n > n_{\max}$, it is assumed that the signal return is so weak that it is impossible to detect anything.

Several methods exist to resolve range ambiguities. One example is performing several measurements with different PRIs and solving the series of equations to acquire the true range. The more targets present, the more equations are required. Another method is to operate with non-repeating waveforms, such as noise waveforms.

The range resolution dr is inversely proportional to the pulse length, that is, high range resolution requires transmitting short pulses. However, if the transmitted pulse is internally modulated, pulse compression – also referred to as matched filtering – can be applied to circumvent the relation between range resolution and pulse length [52, 53]. Let $x_n = x(n/f_s)$ represent the corresponding discrete samples of the reference pulse $x(t)$, where f_s is the baseband sampling rate, and similarly let y_n represent the discrete samples of the received signal $y(t)$. Pulse compression is performed by calculating the cross-correlation ρ_k between the received signal y_n and the conjugated reference signal x_n ,

$$\rho_k = \sum_n y_n x_{n-k}^*, \quad (2.2)$$

where k indexes the range resolution cells and represents the discrete propagation delay, and $\{\cdot\}^*$ denotes the conjugate operation. By performing pulse compression, the range resolution dr is determined by the modulation bandwidth B as

$$dr = \frac{c}{2B}. \quad (2.3)$$

Pulse compression is a powerful tool that combines the energetic advantages of long pulses with the high resolution of short pulses. It is critical for noise radar operation.

In hardware implementations, the cross-correlation is generally calculated in the frequency domain utilizing the fast Fourier transform (FFT) as it is more computationally efficient [53]. Let the vectors $\vec{x} = (x_0, x_1, \dots, x_{M-1})^\top$ and $\vec{y} = (y_0, y_1, \dots, y_{M-1})^\top$ collect a sequence of M samples, where M is the length of the pulse. The cross-correlation is then calculated as

$$\vec{\rho} = \text{IFFT} \left[\text{FFT}(\vec{y}) \odot \text{FFT}(\vec{x}^*) \right], \quad (2.4)$$

where \odot refers to the Hadamard product. This implementation calculates the circular cross-correlation. However, often, the linear cross-correlation is preferred; in that case, the vectors \vec{x} and \vec{y} must be zero-padded.

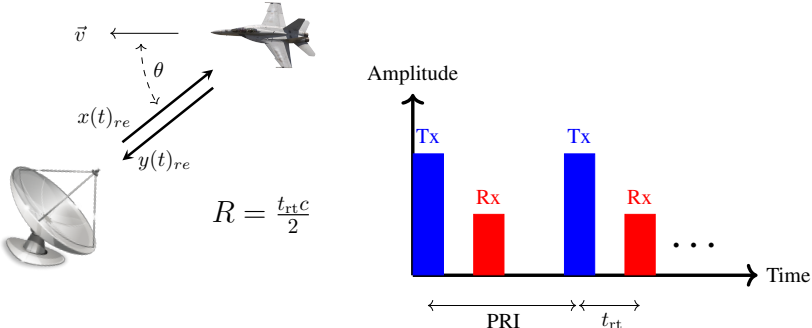


Figure 2.1: **Pulsed Radar Operation** The radar transmits (Tx) a series of pulses $x(t)_{re}$, repeated every pulse repetition interval (PRI) and receives (Rx) the echo signal $y(t)_{re}$. Here $x(t)_{re}$ and $y(t)_{re}$ refers to the real value of $x(t)$ and $y(t)$, respectively. The distance to target R is derived from the pulse's round trip time t_{rt} . The angle θ between the target velocity vector \vec{v} and the vector pointing towards the radar affects the induced Doppler shift; see Eq. (2.5). Credit is given to reference [85] for use of the images.

2.1.2 Velocity Measurement and Velocity Resolution

A coherent radar system – meaning that the phase of the transmitter and receiver is relatively stable – is required [52] to determine the radial velocity v_{ra} of a target. If the system is coherent, the radial velocity is determined by measuring the time-dependent phase difference between the transmitted and the received signal, that is, measuring the induced Doppler shift f_D [53],

$$f_D = \frac{2v_{ra}}{\lambda} = \frac{2v \cos(\theta)}{\lambda}, \quad (2.5)$$

where λ is the wavelength, v_{ra} is the target radial velocity, v is the target velocity, and θ is the angle between the target velocity vector and the vector pointing towards the radar – see Fig. 2.1. Eq. (2.5) describes the non-relativistic Doppler frequency. A coherent and pulsed radar system is often called a pulse-Doppler radar. To coherently process the signal return of a target, the target itself must also remain coherent during the coherent processing interval (CPI). Examples of when the target does not remain coherent over the CPI are shown in appended paper V.

The velocity resolution dv is determined by the Doppler filter bank [52], illustrated in Fig. 2.2. A Doppler filter bank consists of band-pass filters to separate signal components of different frequencies. In the digital domain, a Doppler filter bank is implemented by applying the FFT over several pulses for each range resolution cell – see Fig. 2.3. Since the frequency resolution is $df = 1/T_{int}$, where T_{int} is the coherent integration time, the velocity resolution for a FFT Doppler filter bank is

$$dv = \frac{\lambda}{2T_{int}}. \quad (2.6)$$

If the target radial velocity is between the maximum of two Doppler filters, it

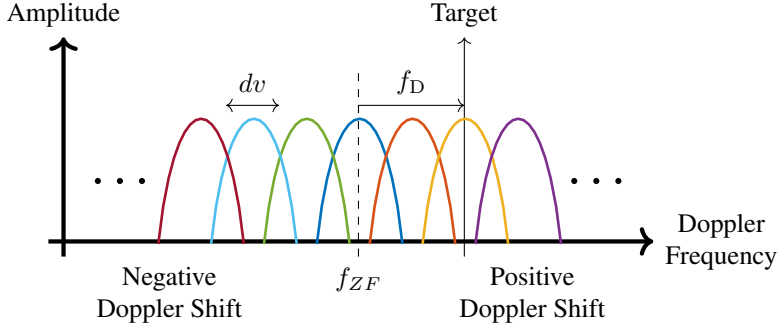


Figure 2.2: Doppler Filter bank A Doppler filter bank consists of several band-pass filters and discriminates between signal components of different frequencies. For example, a target with Doppler shift f_D will enter the yellow filter, whereas reflections from stationary objects fall in the blue zero frequency (ZF) filter. The width of the filters determines the velocity resolution dv .

results in a signal-to-noise ratio (SNR) loss, referred to as scalloping loss [36]. The maximum loss for an FFT Doppler filter bank is roughly 3.9 dB, but if the signal is up-sampled or if a window function is implemented, scalloping losses are reduced. The range processing also suffers from SNR losses – straddling losses – if the actual target range is not in the center of a range resolution cell [36]. Similarly, as with scalloping losses, straddling losses are reduced by up-sampling or windowing.

Doppler processing essentially samples the phase of the received signal with a sampling rate of 1/PRI. Frequency components above half the sampling rate are folded, leading to velocity ambiguities. The maximum unambiguous velocity v_a is λ divided by four times the PRI – the division by 4, instead of 2, is because the direction of the target is unknown. Therefore, the velocity is [53]

$$v = \frac{f_D \lambda}{2 \cos(\theta)} + v_a \cdot n = \frac{f_D \lambda}{2 \cos(\theta)} + \frac{\lambda}{4 \cdot \text{PRI}} \cdot n, \quad n = 0, 1, 2, \dots, \quad (2.7)$$

Observing Eq. (2.1) and Eq. (2.7), it is noted that the range ambiguities are linearly proportional to the PRI, whereas the velocity ambiguities are inversely proportional to the PRI. The product of R_a times v_a is $R_a \cdot v_a = c^2/(8f_c)$, where f_c is the carrier frequency. Thus, pulsed-Doppler radars must choose whether to be unambiguous in range or unambiguous in Doppler. Noise radars do not suffer from such limitations.

2.1.3 Range and Velocity Processing Summarized

Range and velocity processing of pulse-Doppler radars are summarized in Fig. 2.3. Assume P pulses are collected – where each pulse is of length M samples – and that each pulse occupies a row in a matrix. The range information is obtained by cross-correlating all received pulses \vec{y}_p with the reference pulse \vec{x} – referred to as fast time processing. The FFT is then applied over all columns to retrieve the Doppler information, called slow-time processing. This results in a range-Doppler map.

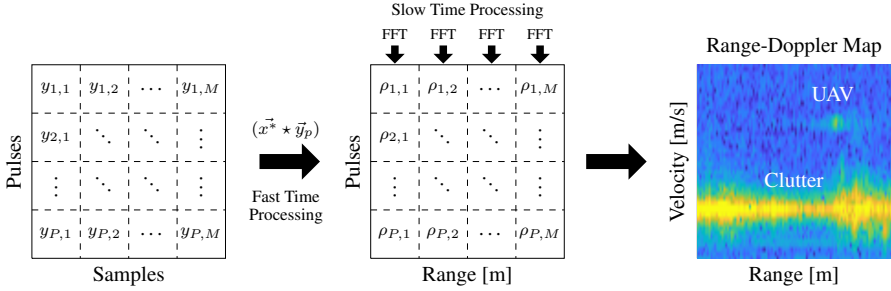


Figure 2.3: **Range-Doppler Processing** Let each of the P received pulses \vec{y}_p occupy a row in a matrix. Each received pulse is then cross-correlated ($\vec{x}^* \star \vec{y}_p$) with the reference pulse \vec{x} , providing the range information. The Doppler information is retrieved by calculating the FFT for each column, resulting in a range-Doppler map. The Doppler processing separates moving objects from the stationary background, allowing for target detection. In the example, a small UAV moving with a velocity of 3 m/s is detected in the presence of strong clutter thanks to the Doppler processing.

The range-Doppler processing can be formalized as an equation. Let $\mathbf{Y}_{p,q}$ represent the discrete Fourier transform of $y_{p,m}$,

$$\mathbf{Y}_{p,q} = \frac{1}{M} \sum_{m=0}^{M-1} y_{p,m} e^{-2\pi i \frac{q \cdot m}{M}}, \quad (2.8)$$

and let \mathbf{X}_q represent the discrete Fourier transform of x_m . Range-Doppler processing is then expressed as

$$\Lambda_{l,m} = \sum_{p=0}^{P-1} \left(\sum_{q=0}^{M-1} \mathbf{Y}_{p,q} (\mathbf{X}_q)^* e^{2\pi i \frac{q \cdot m}{M}} \right) e^{-2\pi i \frac{l \cdot p}{P}}, \quad (2.9)$$

where $\Lambda_{l,m}$ denotes the resolution cell. The formalism will change slightly if zero-padding or up-sampling are used.

2.1.4 Detector – Constant False Alarm Rate

The detector discriminates targets of interest against a background of noise and interference. Generally, for the detector to declare detection, the energy content of a resolution cell under test (CUT) must exceed a detection threshold κ ,

$$|\Lambda_{l,m}|^2 \begin{cases} \stackrel{\mathcal{H}_1}{\gtrless} \kappa & \text{Detection declared} \\ \stackrel{\mathcal{H}_0}{\lessgtr} \kappa & \text{No detection} \end{cases} \quad (2.10)$$

How κ is chosen depends on the detector. Eq. (2.10) describes the square law detector, but there are also other forms of detectors [53].

The type of detectors implemented in this thesis are all square law detectors and all maintain a constant false-alarm rate (CFAR) [53]. A false alarm is an erroneous

detection, indicating a target is present when there is none. False alarms are caused by noise or other interfering signals exceeding the detection threshold. The false alarm rate is the total number of erroneous detections divided by the number of resolution cells under test. The CFAR implementation continuously adapts the threshold to keep the false alarm rate constant. If the statistics of the interfering background are known, for example, Gaussian distributed noise, it is possible to derive a relation between the false alarm rate and the threshold [86].

In appended paper I and V, the detector implemented is a cell-averaging CFAR (CA-CFAR) [53]. A CA-CFAR compares the CUT to the average of several surrounding reference cells. The method by which the reference cells are chosen depends on the implementation. Examples of CA-CFAR implementations are seen in Fig. 2.4. The guard cells in Fig. 2.4 avoid energy leakage from the CUT raising the average of the reference cells. In appended paper I, a diagonal CA-CFAR configuration was applied as it performed best for the noise waveform. In appended paper V, a CA-CFAR with surrounding reference cells was chosen. In appended papers III and IV, a CFAR is maintained by restricting the data rate; see the papers for more information. In appended paper II, detection is performed by visual confirmation of the range-Doppler map.

2.1.5 Angular Resolution and Accuracy

The angular resolution describes the minimum angle between two targets for which the radar can still separate them. Angular accuracy describes the accuracy in the angle estimation for one target. The angular resolution is roughly the 3 dB beam width $\theta_{3\text{dB}}$, which is equal to

$$\theta_{3\text{dB}} = g \frac{\lambda}{d}, \quad (2.11)$$

where d is the dimension of the antenna and g is a constant determined by the shape of the antenna [87]. For a rectangular antenna, $g = 0.88$. The angular accuracy θ_{acc} can be approximated to $\theta_{\text{acc}} \approx \theta_{3\text{dB}}/10 = g\lambda/(10d)$ [87]. However, if the angular accuracy is given a more thorough treatment, it will be seen that the accuracy also depends on the SNR. A higher SNR leads to better accuracy – this is also true for the range and velocity resolution, higher SNR, better resolution.

2.1.6 Radar Range Equation

The radar range equation determines the maximum range R_{\max} for which a specific target can be detected under certain conditions. Alternatively, it can estimate the SNR for a specific target at a certain range. The range equation takes many different forms, depending on definitions and the radar's mode of operation [52, 53]. The form used within this work is

$$R_{\max} = \left(\frac{P_T \delta G_T G_R \lambda^2 T_{\text{int}} \eta}{(4\pi)^3 L k_B F T_0 \kappa} \right)^{\frac{1}{4}}, \quad (2.12)$$

where P_T is the peak transmitted power, δ is the duty cycle, G_T is the transmitter's antenna gain, G_R is the receiver's antenna gain, λ is the wavelength, T_{int} is the integration time, η is the target radar cross section (RCS), k_B is Boltzmann's constant,

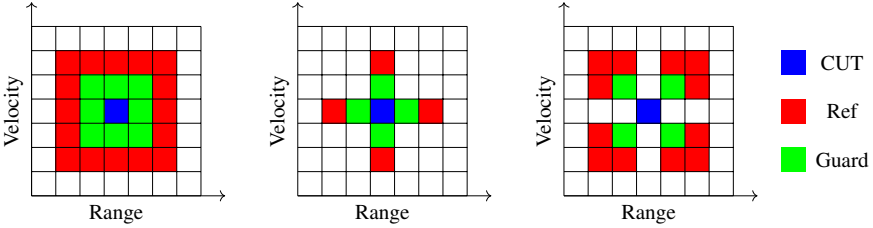


Figure 2.4: Cell Averaging Detectors The cell under test (CUT) is compared to the average of several reference (Ref) cells. A detection is declared if the energy content in the CUT exceeds the reference average by a specific threshold. The reference cells can be chosen in different ways, where three examples are given above. Guard cells – the cells between the CUT and reference cell – are often used to mitigate the risk of energy leakage from the CUT raising the reference average.

T_0 is the standard temperature of 290 K, F is the receiver's noise figure, κ is the detection threshold and L are the overall losses, which includes processing losses, atmospheric absorption losses, receiver losses, etc. The equation assumes that receiver bandwidth is approximately equal to the bandwidth of the waveform. If that is not the case, the equation has to be modified. In continuous wave (CW) systems, the duty cycle always equals $\delta = 1$.

This work mainly uses the radar range equation to verify the measurement results, confirm that the SNR is roughly equal to the expectations, and conclude whether the system is noise-limited or clutter-limited.

2.1.7 Bistatic Radar

The above discussion assumes that the radar is monostatic; most radar systems are, after all, monostatic. Monostatic radar means that the transmitter and receiver are located at the same site, allowing both units to be disciplined by the same reference oscillator, leading to excellent synchronization in time and frequency. Quite often, the same antenna is also used for both transmission and reception.

In bistatic radar systems [84, 88], the transmitter and receiver are separated by a considerable distance, resulting in the radar system operating with more complicated characteristics, and synchronization between the receiver and transmitter is challenging to achieve as different reference oscillators discipline the two. There are also monostatic configurations where the receiver and transmitter are located at the same site and are disciplined by the same oscillator but have separate antennas. Such systems are sometimes referred to as quasi-monostatic [53]. In this thesis, the notation of monostatic and bistatic is used to refer to whether the transmitter and receiver are synchronized by the same oscillator or by different oscillators.

The systems implemented and described in appended paper I, IV, and appended paper V are examples of bistatic systems. Monostatic and bistatic radar are relatively similar if detailed technical aspects are ignored. Essential differences are slight changes in the radar range equation and the induced Doppler shift – these differences are shown in appended paper I.

2.2 Noise Radar

The primary difference between a noise radar and a pulse-Doppler radar is that the noise radar, as the name suggests, transmits random or pseudorandom noise-like waveforms. A noise radar can operate both in a continuous wave mode or a pulsed mode, it can transmit a narrow band or a broadband waveform, which can repeat or be non-repeating. Although noise radars can operate in a multitude of different modes, it is almost always assumed that they operate with broadband pulses, transmit and receive continuously, integrate for a long time (longer than traditional pulsed radars), and transmit non-repeating pulses since such a mode of operation is important for LPI properties [5].

Operating a broadband noise radar system is challenging and requires specialized signal processing. This section introduces the signal processing necessary for broadband noise radar operation. Much of the signal processing introduced can also be applied to several other waveforms. First, one example of pseudorandom waveform generation is explained. Then, the cross ambiguity function (CAF), used to calculate the range and velocity, is introduced. Next, the main fundamental problem of noise radar operation, that is, the CNF problem, is detailed. Then, an efficient range-Doppler processing for noise radars is presented. Calculating the CAF is not efficient enough for real-time implementation, so more efficient methods are required. Fourth, an expression for the Doppler tolerance of noise waveforms is derived. Fifth, the moving target compensation, required if operating with high time-bandwidth products, is specified. Lastly, two clutter suppression algorithms are presented.

2.2.1 Waveform Generation – Linear Feedback Shift Registers

Several different methods can generate noise-like waveforms. In this thesis, all noise waveforms are generated in the digital domain by linear feedback shift registers (LFSR) [89], using built-in Matlab functions [90]. The operation of an 8-bit example shift register is shown in Fig. 2.5 as an example. The input to the register is driven by the XOR of some of the bits from the overall shift register value; these bits are called taps. LFSRs generate pseudorandom noise, not true random noise, and there have been some critiques that this would deteriorate LPI performance [91]. Also, using LFSRs creates waveforms with high amplitude modulation and, consequently, a high peak-to-average power ratio (PAPR). To increase the efficiency of the amplifier, operating with a low PAPR is preferred. Low PAPR noise waveforms are under investigation by other research groups [6, 64–66] and are outside the scope of this thesis.

The maximum length – the number of binary samples before repetition – of a l -stage LFSR is $2^l - 1$. Accounting for that b binary samples are required to form a b -bit sample, the repetition time t_{rep} of a LFSR is

$$t_{\text{rep}} = \frac{2^l - 1}{bf_s}. \quad (2.13)$$

For example, with a baseband sampling rate of $f_s = 250$ MHz, a bit depth of $b = 16$ -bits, and a polynomial length of $l = 53$, the repetition time is about 26 days – practically an eternity in radar operation. However, an ESM receiver only requires $2l - 1$ samples to break the sequence due to the linear properties of the generator [89].

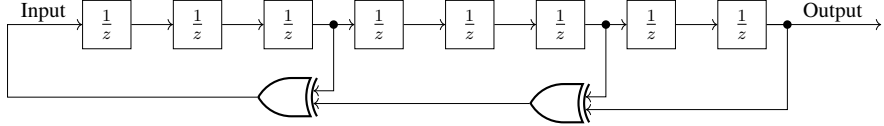


Figure 2.5: Linear feedback shift register This is an example of an 8-bit linear feedback shift register (LFSR), where the feedback from two XOR gates determines the register's input. Each box represents a unit delay, and the bits are cyclically shifted at each time interval of $1/f_s$. The LFSR creates a pseudorandom output signal.

On the other hand, a radar signal can not be compared with a telecommunications signal, where all the bits are error-corrected. Aside from the actual signal, the radar signal will contain a fair amount of noise, interference, non-linearities, and other disturbances, and breaking the sequence will likely be very difficult. Additionally, several pseudorandom sequences can be combined non-linearly, and the sequences used can be frequently altered – only imagination limits the complexity. From a practical view, pseudorandom noise does not deteriorate LPI properties.

The spectrum of the output from the LFSR is white noise spanning the Nyquist bandwidth. To obtain an appropriate signal bandwidth, the LFSR output is filtered by a finite impulse response (FIR) filter – referred to as noise filter in Fig. 1.1 – creating a complex band-pass limited noise signal.

2.2.2 Cross Ambiguity Function

The cross ambiguity function (CAF) is a two-dimensional function of the propagation delay k and the Doppler frequency f_D . It represents the response of the matched filter (Eq. (2.2)) for all delays and Doppler shifts. For a complex baseband pulse, the discrete cross-ambiguity function $\chi_{k,v}$ is

$$\chi_{k,v} = \sum_n y_n x_{n-k}^* \cdot e^{2\pi i (2v_{ra} f_c/c) \cdot \frac{n}{f_s}}. \quad (2.14)$$

The received signal is cross-correlated with a Doppler-shifted reference signal for all velocities of interest. For a waveform with a high time-bandwidth product, calculating the CAF is very inefficient, and instead, range and Doppler are calculated similarly to pulse-Doppler radars – see subsection 2.2.4.

The range and Doppler response for a single-point reflector is determined by calculating the CAF for $y_n = x_n$. A qualitative comparison – meaning that the waveform parameters are not equal – between the commonly used chirp waveform [52, 53] and a noise waveform with a rectangular frequency spectrum – see Fig. 2.6 (e) – is seen in Fig. 2.6 (a) and Fig. 2.6 (b), respectively. The chirp has significant coupling between range and Doppler, whereas the noise waveform does not. It is said that the chirp is Doppler tolerant, meaning a Doppler shift will not result in an SNR loss. Unlike the chirp, noise waveforms have low Doppler tolerance, resulting in SNR losses for Doppler shifted signals – this is further detailed in subsection 2.2.5. In the author's opinion, low Doppler tolerance is primarily a disadvantage. However, if the more practical signal processing in subsection 2.2.4 is implemented, Doppler tolerance is rarely of concern.

The noise waveform in Fig. 2.6 (b) exhibits strong deterministic sidelobes in both range and Doppler. The sidelobes in Doppler are caused by discontinuities at the edges of the waveform and can be mitigated by time-domain windowing. In Fig. 2.6 (c), a Hann window is applied, and the sidelobes in Doppler are consequently suppressed. The level of sidelobe suppression depends on the window of choice. Windowing, however, also results in an SNR loss and lower velocity resolution – visible in Fig. 2.6 (c) as the main peak widens. Choosing a window that provides enough sidelobe suppression while minimizing the loss in SNR is an important consideration in most system designs. In this thesis, little thought is given to choosing the perfect window, and the Hann window is applied as it is considered good enough. For a Hann window, the SNR loss is about 1.8 dB.

The range sidelobes depend on the shape of the frequency spectrum, and what is seen in Fig. 2.6 (b) is the result of the convolution of two pulses with a rectangular spectrum. In Fig. 2.6 (d), the range sidelobes are suppressed by applying a frequency domain window, resulting in a Gaussian-like frequency spectrum or a spectrum with soft edges – see Fig. 2.6 (f). In appended paper I, the prominent sidelobes in range are due to the rectangular shape of the frequency spectrum. Apart from appended paper I, noise waveforms with a more soft frequency spectrum are always utilized to suppress range sidelobes.

For a soft frequency spectrum, an equivalent noise bandwidth (ENBW) is defined as the bandwidth of a perfect rectangular filter that produces the same integrated noise power as that of the actual filter [92], that is,

$$\text{ENBW} = f_s \frac{\sum_n |h_n|^2}{\left| \sum_n h_n \right|^2}, \quad (2.15)$$

where h_n is the taps of the FIR filter. The effective bandwidth of a soft frequency spectrum is illustrated in Fig. 2.6 (f) with a red dashed line.

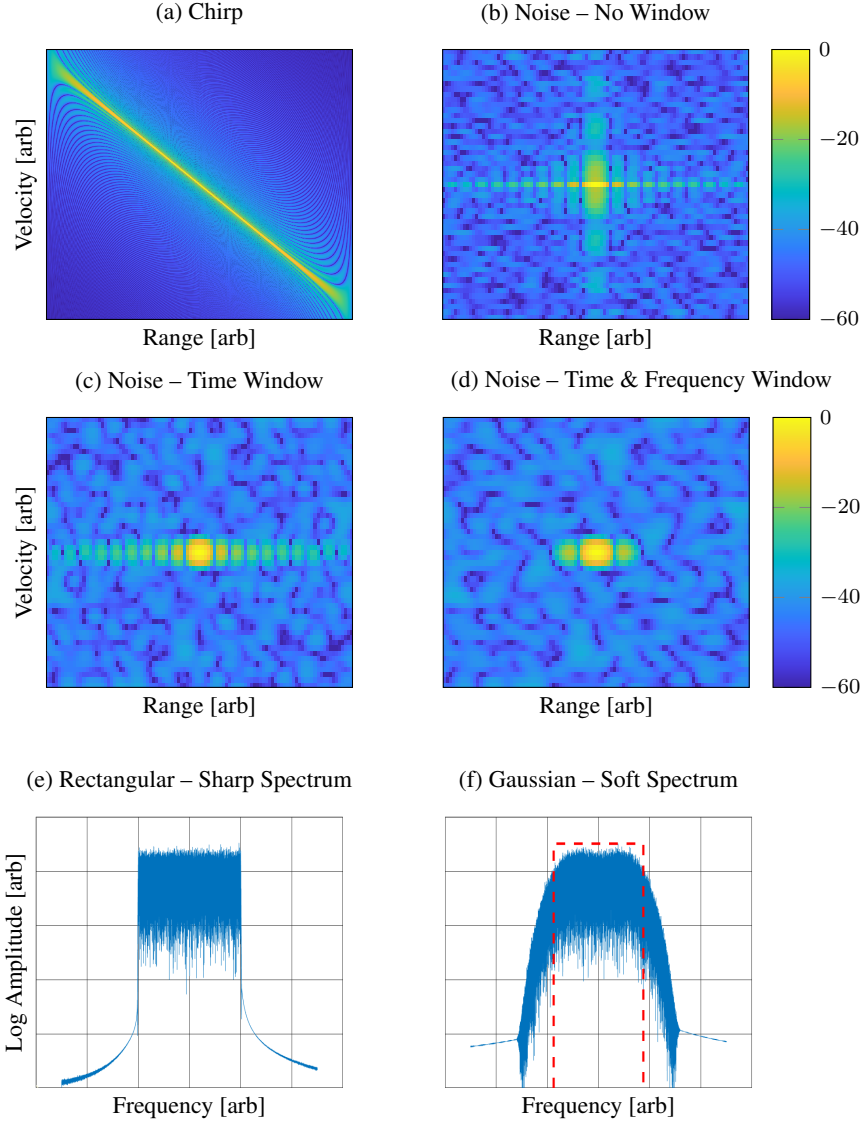


Figure 2.6: Ambiguity Functions Illustration of the ambiguity function for (a) A chirp. (b) Noise waveform with high deterministic range and Doppler sidelobes. The range sidelobes are due to the rectangular shape of the frequency spectrum, see (e), and the Doppler sidelobes are due to the discontinuities at the edges of the waveform. (c) A noise waveform with a time-domain window applied, which suppresses the Doppler sidelobes. (d) Noise waveform with both a time domain and frequency domain window applied – see the resulting frequency spectrum in (f) – suppressing both range and Doppler sidelobes. The chirp and noise waveform parameters are unequal, and only qualitative comparisons should be made. For more Gaussian-like spectrums, as in (f), an effective bandwidth is defined according to Eq. (2.15). The effective bandwidth for the spectrum in (f) is illustrated with a dashed red line.

2.2.3 Correlation Noise Floor – Masking Effect

Further observing Fig. 2.6, it is clear that the noise waveform suffers from a uniform residual noise floor, that is, the CNF. The variance of the CAF determines the CNF level. To convey the concept, it is sufficient to derive an expression for the variance of the auto-correlation function – the zero velocity range cut of the CAF with $y_n = x_n$. The derivation closely follows work by S. Axelsson [33, 57]. Assume x_n is a complex signal of N uncorrelated samples and that it is sampled from a normal distribution with zero mean and variance σ^2 , that is, $x_n \sim \mathcal{CN}(0, \sigma^2)$. The auto-correlation is defined as

$$\rho_k = \sum_n x_n x_{n-k}^*, \quad (2.16)$$

and the variance of the auto-correlation σ_S^2 is given by

$$\begin{aligned} \sigma_S^2 &= \mathbb{E}[|\rho_k|^2] - |\mathbb{E}[\rho_k]|^2 = \\ &\mathbb{E}\left[\sum_{n=1}^{N-1} x_n x_{n-k}^* \sum_{r=1}^{N-1} x_r^* x_{r-k}\right] - \left|\frac{1}{N} \sum_{k=1}^{N-1} \sum_{n=1}^{N-1} x_n x_{n-k}^*\right|^2, \end{aligned} \quad (2.17)$$

where $\mathbb{E}[\cdot]$ denotes the expectation value. Generally, the variance outside the main lobe is of interest, that is, $k \neq 0$, for which x_n and x_{n-k} are uncorrelated. The statistical distribution of $x_n x_{n-k}^*$ for $k \neq 0$ results in a zeroth order Bessel function of the second kind [93], also with zero mean. Hence, the summation over all samples in the second term equals zero. The first term is simplified by applying the general distributively theorem of summations and the linear property of the expectation value:

$$\sigma_S^2 = \mathbb{E}\left[\sum_{n=1}^{N-1} \sum_{r=1}^{N-1} x_n x_{n-k}^* x_r^* x_{r-k}\right] = \sum_{n=1}^{N-1} \sum_{r=1}^{N-1} \mathbb{E}\left[x_n x_{n-k}^* x_r^* x_{r-k}\right]. \quad (2.18)$$

Only the terms for which $r = n$ are nonzero, and since x_n and x_{n-k} are independent processes for $k \neq 0$

$$\sigma_S^2 = \sum_{n=1}^{N-1} \mathbb{E}\left[|x_n|^2 |x_{n-k}|^2\right] = \sum_{n=1}^{N-1} \mathbb{E}\left[|x_n|^2\right] \mathbb{E}\left[|x_{n-k}|^2\right]. \quad (2.19)$$

Since x_n is of zero mean $\mathbb{E}[|x_n|^2] = \mathbb{E}[|x_{n-k}|^2] = \sigma^2$. The resulting auto-correlation variance is then

$$\sigma_s^2 = N\sigma^4, \quad \text{If } k \neq 0. \quad (2.20)$$

If $k = 0$, the auto-correlation is

$$\rho_0 = \sum_n x_n x_n^* = \sum_n |x_n|^2. \quad (2.21)$$

For high time-bandwidth products ($N = BT_{\text{int}} \gg 1$), the peak value of the auto-correlation is close to its mean value of $N\sigma^2$. Hence, the peak-to-average sidelobe ratio (PASR) is

$$\text{PASR} = \frac{(N\sigma^2)^2}{\sigma_s^2} = N. \quad (2.22)$$

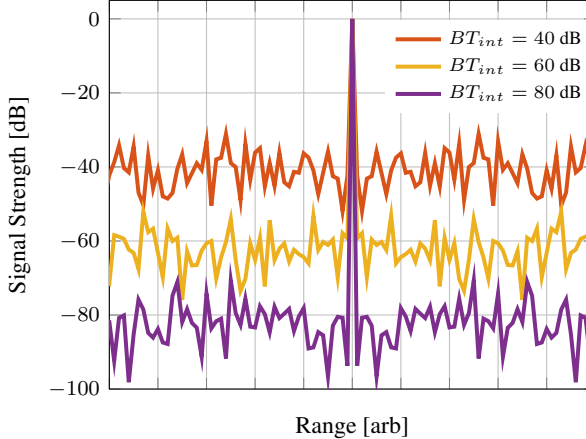


Figure 2.7: Correlation Noise Floor The auto-correlation of a noise waveform for different time-bandwidth products (BT_{int}) illustrates that the average sidelobe level is roughly the time-bandwidth product below the main peak. Hence, a large time-bandwidth product is beneficial for suppressing the correlation noise floor.

High bandwidth and long integration times are beneficial for suppressing the CNF but introduce other difficulties – covered in subsection 2.2.6. The auto-correlation for different time-bandwidth products is shown in Fig. 2.7.

2.2.4 Efficient Range-Doppler Processing – Batched Processing

Calculating the CAF for large time-bandwidth products requires significant computational resources, constraining the CAF to offline processing. For real-time noise radar operation, a more resource-efficient signal processing is required, for example, batched processing [33, 36, 94]. Batched processing is inspired by pulse-Doppler radar processing. The reference waveform x and the received signal y , consisting of N samples, are segmented into P batches of length M samples. Similarly to the range-Doppler processing in Fig. 2.3, each batch occupies a row in the matrix, with the minor difference that there now are two matrices, one for the signal $y_{p,m}$ and one for the reference $x_{p,m}$, and the range information is now obtained by cross-correlating \vec{y}_p and \vec{x}_p . The rest of the signal processing, that is, velocity calculation, detection, tracking, etc., remains the same as for pulse-Doppler radars. The batched processing can be formalized as

$$\Lambda_{l,m} = \sum_{p=0}^{P-1} \left(\sum_{q=0}^{M-1} \mathbf{Y}_{p,q} (\mathbf{X}_{p,q})^* e^{2\pi i \frac{q \cdot m}{M}} \right) e^{-2\pi i \frac{l \cdot p}{P}}. \quad (2.23)$$

Comparing Eq. (2.23) and Eq. (2.9), it can be seen how the batched processing is inspired by the pulse-Doppler radar processing. Batched processing is the signal processing implemented in all appended papers.

Batched processing introduces an effective PRI equal to the batch length t_p , $\text{PRI} = t_p = M/f_s$, resulting in Doppler ambiguities – see Eq. (2.7). However, the

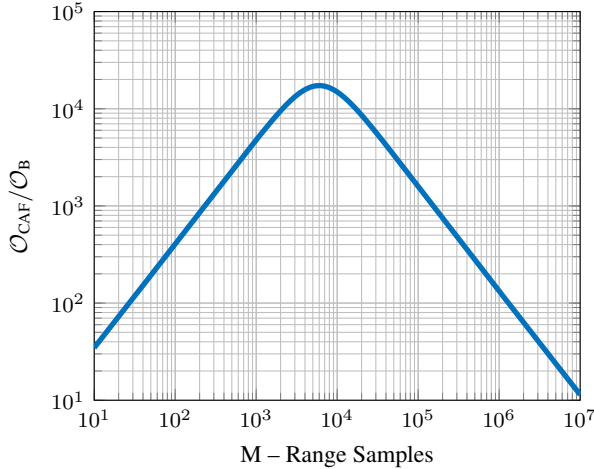


Figure 2.8: **Computational Calculations** The ratio of the number of calculations required to calculate the CAF, \mathcal{O}_{CAF} , and the number of calculations required for the batch processing, \mathcal{O}_B . The example is for $V = 1$ and a time-bandwidth product of 80 dB, illustrating the computational advantage of batched processing.

batch length can be chosen arbitrarily, allowing for parallel or sequential processing of different PRIs to resolve the Doppler ambiguities – this requires an increase in computations. However, the noise radar is still ambiguity-free in range and, therefore, has much greater freedom in choice of PRI than pulse-Doppler systems.

Based on the results in subsection 2.2.3, it is known that the cross-correlation of each batch results in a PASR = M . Considering the sidelobes are randomly distributed values, the FFT in the Doppler dimension results in a white spectrum, that is, the energy is spread out uniformly in the Doppler dimension, and the total PASR is PASR = $M \cdot P = N = BT_{\text{int}}$. This is a qualitative explanation as to why the CNF follows the time-bandwidth product despite applying Doppler processing.

The number of operations required for calculating the FFT scales as $\mathcal{O}(n \log_2 n)$ [95], pairwise multiplication scales as $\mathcal{O}(n)$, and complex conjugate is assumed to be for free. Performing the batched processing, then scale as

$$\mathcal{O}_B(3 \cdot M \log_2(M) + P \log_2(P) + M), \quad (2.24)$$

and calculating the CAF scales as

$$\mathcal{O}_{\text{CAF}}(3 \cdot VPM \log_2(PM) + VPM), \quad (2.25)$$

where V is the number of velocities the CAF is calculated for. For high time-bandwidth products, the difference between \mathcal{O}_{CAF} and \mathcal{O}_B is substantial. For example, assume $V = 1$ and that the time-bandwidth product is 80 dB, that is, $N = PM = 10^8$, then $\mathcal{O}_{\text{CAF}}/\mathcal{O}_B$, as a function of M , is shown in Fig. 2.8. The maximum difference is $\approx 2 \cdot 10^4$, and that is for $V = 1$. Usually, V will be several orders of magnitude larger than 1. It should now be clear why calculating the CAF is not preferable.

Another more practical aspect of performing batch processing is that most pre-defined FFT routines available in different hardware description languages (HDLs) have a maximum sample length of $2^{16} = 65336$. Using the predefined routines to calculate the CAF will limit the time-bandwidth product to $10 \log_{10}(2^{16}) \approx 45$ dB, whereas time-bandwidth products of $10 \log_{10}(2^{16} \cdot 2^{16}) \approx 90$ dB is possible with batched processing.

2.2.5 Doppler Tolerance

Doppler tolerance refers to how sensitive the cross-correlation of a certain waveform is to an induced Doppler shift. Subsection 2.2.2 showed that a noise waveform has low Doppler tolerance and that the cross-correlation might get a significant SNR loss due to a Doppler shift. Compensating for the induced Doppler shift is relatively trivial; a Doppler modulation is applied to the reference signal as

$$x'_n = x_n \cdot e^{-2\pi i (2v_r f_c/c) \cdot \frac{n}{f_s}}, \quad (2.26)$$

where v_r is the assumed target radial velocity. Since the target radial velocity is usually unknown, several hypotheses of v_r might have to be calculated in parallel or sequentially.

The resulting loss L_D is defined as [50]

$$L_D = \frac{|\chi_{0,0}|^2}{|\chi_{k,v}|^2} = \frac{|\chi_{0,0}|^2}{|\chi_{0,v}|^2}, \quad (2.27)$$

where the value of k , due to the lack of range-Doppler coupling, is set to $k = 0$. Substituting $f_D = 2v_{ra}f_c/c$ and setting $y_n = x_n$, results in

$$\begin{aligned} \chi_{0,v} &= \sum_{n=0}^{N-1} x_n x_n^* \cdot e^{2\pi i f_D \cdot \frac{n}{f_s}} = \sum_{n=0}^{N-1} |x_n|^2 \cdot e^{2\pi i f_D \cdot \frac{n}{f_s}} = \\ &\quad \sum_{n=-\infty}^{\infty} |x_n|^2 \cdot e^{2\pi i f_D \cdot \frac{n}{f_s}} \cdot e_n \end{aligned} \quad (2.28)$$

where e_n defines the time window function, here assumed to be rectangular:

$$e_n = \begin{cases} 1 & \text{if } n = 0, 1, \dots, N-1 \\ 0 & \text{otherwise} \end{cases} \quad (2.29)$$

A rectangular time domain window is always applied because the sequence is always finite. The definition of e_n implies that $|x_n|^2 \cdot e_n = |x_n e_n|^2$. Eq. (2.28) is identified as the discrete Fourier transform of $|x_n|^2 \cdot e_n$, and applying the convolution theorem results in

$$\chi_{0,v} = \mathcal{F}(|x_n|^2) \star \mathcal{F}(|e_n|) = \chi_{0,0} \cdot \mathcal{F}(|e_n|), \quad (2.30)$$

where $\mathcal{F}(|x_n|^2) \approx \chi_{0,0}$ for high time bandwidth products [50, 96]. Hence, the loss L_D only depends on the time window function, $L_D = |\mathcal{F}(|e_n|)|^{-2}$. For a rectangular window of length t_p , the loss is defined by the inverse of the $\text{sinc}(\pi f_D t_p)$ function:

$$L_D = \left| \frac{\sin[2\pi f_c(v_{ra} - v_r)t_p/c]}{2\pi f_c(v_{ra} - v_r)t_p/c} \right|^{-2}. \quad (2.31)$$

If a maximum loss L_D of 3 dB is acceptable, the maximum velocity mismatch for a rectangular window is roughly

$$|v_{ra} - v_r|_{\max} \approx \frac{0.22c}{t_p f_c}. \quad (2.32)$$

If running multiple hypotheses, the required velocity spacing is $2|v_{ra} - v_r|_{\max}$. For a carrier frequency of $f_c = 1.3$ GHz and a batch length of $t_p = 10 \mu\text{s}$, the maximum velocity mismatch allowed is about $|v_{ra} - v_r|_{\max} = 5000 \text{ m/s} = 18000 \text{ km/h}$

In this thesis, the batch lengths and target velocity are often low enough not to require Doppler compensation. The exception is in appended paper II, where the batch length is chosen to be extreme in order to study a Doppler loss. If time-domain windowing is applied, for example, a Hann window, the requirements are relaxed. The maximum velocity mismatch if a time-domain Hann window is applied is about $(v_{ra} - v_r)_{\max} = 10600 \text{ m/s}$ – this is based on simulations.

The Doppler loss is most likely negligible for most applications. However, if operating at higher frequencies or a very low loss is desired, Doppler compensation might have to be applied. It is important to consider the loss mechanism when designing the system.

2.2.6 Range-Walk and Doppler Spread

If the distance a target moves during a CPI is greater than that of a range-resolution cell, the energy return from that target is spread in the range dimension, called range walk, bin migration, or cell migration. An upper limit of the maximum integration time for a target moving with radial velocity v_{ra} before a loss occurs due to range-walk is given by the range resolution dr ,

$$T_{\max} = \frac{dr}{v_{ra}} = \frac{c}{2Bv_{ra}}. \quad (2.33)$$

Doppler spread occurs because the target accelerates and because the Doppler shift varies over the waveform bandwidth. If the frequency resolution is smaller than the Doppler shift variation, energy is spread in the Doppler dimension. The maximum integration time before Doppler spread occurs for a target moving with constant velocity also follows Eq. (2.33). For accelerating targets, the spread is determined by the acceleration and the frequency resolution.

The effect of range-walk and Doppler spread for targets moving with constant velocity is illustrated in Fig. 2.9 for a time-bandwidth product of 87 dB. In Fig. 2.9 (a), the target is stationary, and the energy is concentrated to one resolution cell, whereas in Fig. 2.9 (b), it is moving with $v_{ra} = 10 \text{ m/s}$, resulting in significant spreading and a loss L_S of about 30 dB.

The loss L_S is approximately equal to the total number of resolution cells the energy is spread over [36],

$$L_S = K_R K_D = \frac{v_{ra} T_{\text{int}} 2B}{c} \cdot \frac{v_{ra} T_{\text{int}} 2B}{c} = \frac{4v_{ra}^2 T_{\text{int}}^2 B^2}{c^2}, \quad (2.34)$$

where K_R is the number of range cells, and K_D is the number of Doppler cells. Substituting v_{ra} for the velocity mismatch $(v_{ra} - v_r)$ the loss is

$$L_S = 4(v_{ra} - v_r)^2 (T_{\text{int}} B)^2 / c^2. \quad (2.35)$$

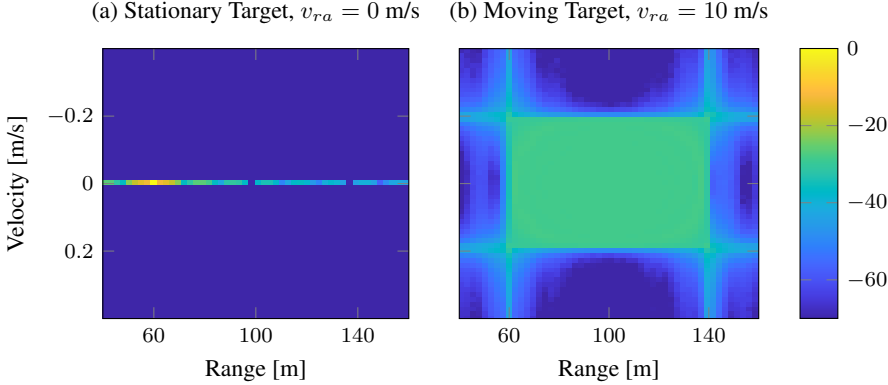


Figure 2.9: **Range-Walk and Doppler Spread Example** Range-Doppler processed data with a time-bandwidth product of 87 dB, for (a) a stationary target, $v_{ra} = 0$ m/s, and (b) a moving target, $v_{ra} = 10$ m/s. The spreading of energy in range and Doppler in (b) results in a significant signal loss of about 30 dB. The simulated example illustrates the importance of compensating for moving targets when operating with high time-bandwidth products.

For high time-bandwidth products, the loss is significant even for very small velocity mismatches – as illustrated by Fig. 2.9 – and operating with high time-bandwidth products requires that the target’s movement is compensated for. The obvious problem is that, as in subsection 2.2.5, the target’s velocity is unknown, and multiple hypotheses are required. Again, if a maximum loss of 3 dB is considered acceptable, the required velocity spacing Δv as a function of different time-bandwidth products is given by

$$\Delta v = \frac{\sqrt{2}c}{BT_{\text{int}}}. \quad (2.36)$$

For a time-bandwidth product of 87 dB, a spacing of about 0.85 m/s is required. Hence, operating with very high time-bandwidth products is a challenging task.

Appended paper II details the implementation of an efficient and FPGA-suitable algorithm [36, 97], which is then implemented in the real-time processor. Essentially, the moving target compensation algorithm performs time-translation in slow time by utilizing the property that $\mathcal{F}[f(n - a)] = \mathcal{F}[f(n)] e^{-\frac{2\pi i}{N}ka}$. In other words, time translation equals a phase ramp in the frequency domain. Between batches, the Fourier transformed reference $\mathbf{X}_{p,q}$ is shifted with the factor $a = 2v_r f_s t_p p / c$, as

$$\mathbf{X}'_{p,q,r} = \mathbf{X}_{p,q} e^{-2\pi i \frac{q \cdot p}{M} \frac{2v_r f_s t_p}{c}} = \mathbf{X}_{p,q} e^{-2\pi i q \cdot p \frac{2v_r}{c}}, \quad (2.37)$$

where it is utilized that $t_p = M/f_s$. The final form of the range-Doppler processing equation is then

$$\Lambda_{l,m,r} = \sum_{p=0}^{P-1} \left(\sum_{q=0}^{M-1} \mathbf{Y}_{p,q} (\mathbf{X}'_{p,q,r})^* e^{2\pi i \frac{q \cdot m}{M}} \right) e^{-2\pi i \frac{l \cdot p}{P}}. \quad (2.38)$$

Doppler spread due to target acceleration is relevant in appended paper V. A chirp [53], corresponding to a linear increase or decrease in frequency, is applied in slow time to compensate for the acceleration.

The Keystone transformation [97–101] is another method that compensates for range-walk and Doppler spread. The advantage of Keystone transformation is that it simultaneously compensates for all unambiguous velocities by resampling in slow-time. The disadvantage is increased computation and a much more complicated implementation. Hence, the Keystone transform was not studied within this thesis. However, for future work/systems, the Keystone transform should be considered.

2.2.7 Clutter Suppression – CLEAN and Lattice Filter

The idea behind clutter suppression algorithms is to estimate the contribution from point scatterers and use these estimates to filter the received signal adaptively. If the contribution of a point scatterer is successfully subtracted from the received signal, it is like it never existed in the first place. Hence, the point scatterer no longer contributes to the CNF. If enough point scatterers are sufficiently suppressed, the CNF is drastically lowered, and the detection sensitivity is significantly increased.

In the preparatory work for appended paper I, two clutter reduction algorithms were investigated: the CLEAN algorithm [102–104] and the lattice filter algorithm [35, 105]. None of the algorithms performed well on their own – see subsection 4.1. However, combining the two, referred to as *sequential CLEAN*, achieved good results. This subsection provides more details about the algorithms. The author did not perform the specifics of the implementations; that credit is given to R. Jonsson (Saab) [71].

As in appended paper I, assume that the received signal y_n is defined by the following model

$$y_n = \alpha x_{n-k} e^{2\pi i (2v_{ra} f_c / c) \frac{n}{f_s}} + \sum_{\substack{k \in \{\text{range}\} \\ j \in \{\text{Doppler}\}}} \beta_{k,j} x_{n-k} e^{2\pi i (2v_j f_c / c) \frac{n}{f_s}} + \nu_n, \quad (2.39)$$

where ν_n is internal receiver noise, v_j is the clutter velocity, α is the target amplitude and $\beta_{k,j} \in \mathbb{C}$ describes the amplitude of point scatters at distance k with velocity v_j . The task for almost all clutter reduction algorithms is to estimate all coefficient $\beta_{k,j}$ that has a notable contribution to the CNF – it is assumed that the target's contribution to the CNF is negligible. In practice, the coefficients are not perfectly estimated – this depends on many factors, such as the model itself being flawed, the world not being a set of discrete point scatters, non-linearities in the radar, etc. Due to the coefficient mismatch, a residue of each point scatterer remains. The remaining residue will determine the resulting CNF level and the algorithm's efficiency.

The CLEAN algorithm is described below under Algorithm 1. The reference x_n and the signal y_n are cross-correlated, and the delay corresponding to the maximum is found. For that delay, the clutter coefficient $\beta_{k,j}$ is estimated for zero-Doppler and a set of surrounding Doppler cells J . The steps are repeated until a stop criterion is fulfilled – this can be a maximum number of iterations, or it is stopped when the overall noise floor no longer decreases, either due to the model mismatch being too large or because clutter is sufficiently suppressed and the detection sensitivity is thermal noise limited.

Algorithm 1 The CLEAN algorithm implemented. The stop criteria is either that a maximum number of iterations has been performed or that the noise floor no longer decreases, that is, the sidelobe level of ρ_k remains constant.

1. Cross-correlate y_n and x_n : $\rho_k = \sum_n y_n x_{n-k}^*$
 2. Find delay k for the maximum: $\text{argmax}_k |\rho_k|$
 3. Estimate $\beta_{k,j}$ for $j \in \{-J, \dots, 0, \dots, J\}$: $\beta_{k,j} = \frac{\sum_n y_n^* x_{n-k} e^{i2\pi n j / N}}{\sum_n x_{n-k} x_{n-k}^*}$
 4. Subtract $\beta_{k,j}$ from y_n : $y_n = y_n - \beta_{k,j}^* x_{n-k} e^{i2\pi n j / N}$
 5. Repeat till stop criteria is fulfilled.
-

The lattice filter structure is described below under Algorithm 2. The lattice filter algorithm aims at creating an orthogonal clutter subspace by subtracting the non-orthogonal components for each range cell. It is a simplified form of the Gram-Schmidt process, utilizing the fact that each range cell already has a high level of orthogonalization due to the noise waveform. In Algorithm 2 x^f and x^b are the forward and backward projection errors. The backward projection error vector forms an orthogonal basis. Utilizing the orthogonal basis, the clutter coefficient $\beta_{k,j}$ is estimated and subtracted from the received signal y_n . x^f and x^b are updated on every iteration based on their partial correlation K .

Algorithm 2 The lattice filter algorithm. The algorithm performs a fixed number of iterations.

```

 $x_n^f \leftarrow x_n$ 
 $x_n^b \leftarrow x_n$ 
while running do
     $\beta_{k,j} \leftarrow \frac{\sum_n y_n^* x_n^b e^{i2\pi n j / N}}{\sum_n x_n^b (x_n^b)^*}$ 
     $y_n \leftarrow y_n - \beta_{k,j}^* x_n^b e^{i2\pi n j / N}$ 
     $K \leftarrow \frac{-2 \sum_n (x_n^f)^* x_{n-1}^b}{\sum_n x_n^f (x_n^f)^* + \sum_n x_{n-1}^b (x_{n-1}^b)^*}$ 
     $x_n^f \leftarrow x_n^f + K \cdot x_{n-1}^b$ 
     $x_n^b \leftarrow x_{n-1}^b + K^* \cdot x_n^f$ 
end while

```

The *Sequential CLEAN* algorithm performs steps 1 and 2 of Algorithm 1 and runs a few iterations of Algorithm 2, usually 2 to 3 iterations. The steps are repeated until a given stop criteria is fulfilled. CLEAN is believed to work well for point-like clutter, and the lattice filter is believed to work well for homogeneous clutter. The combination thus performs better in situations with distributed clutter.

2.3 Beamforming

Beamforming is a technique for directional transmission and reception and is another method applied within the thesis to suppress the CNF. By applying phase weight to the signals received at each antenna element, it is possible to control the antenna diagram

to maximize the gain in specific directions and minimize the gain in other directions – Fig. 2.10 illustrates a typical beamformer. The main lobe is steered toward different directions by applying phase weights w_n according to

$$w_n = e^{-i\pi n \sin(\phi)} \quad (2.40)$$

where it is assumed that the antenna elements are spaced by $\lambda/2$ and ϕ is the direction (angle) of the main lobe.

If a strong interfering signal is present from a specific angle of arrival, it is possible to adaptively cancel that interference by applying advanced beamforming techniques. In appended paper IV, the implementation of a CAPON beamformer [106] is detailed and applied to suppress strong self-interference. One of the advantages of bistatic separation is the ability to apply beamforming to suppress strong self-interference and thereby mitigate the CNF – this is shown in appended paper IV.

The CAPON beamformer is a narrowband technique. An interfering signal is considered narrowband if the rank of the signal subspace is one in the covariance matrix. If so, phase weights and true time delays can be applied interchangeably. For example, phase shifting a sine wave is equivalent to a time delay. In reference [107], narrowband is defined as a function of fractional bandwidth, instantaneous SNR, number of antenna elements, and angle-of-arrival.

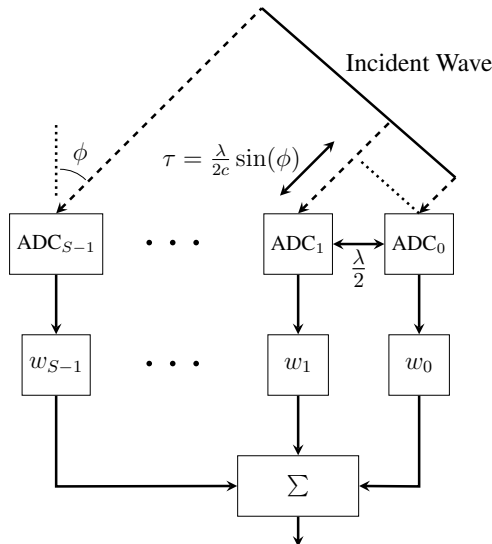


Figure 2.10: **Digital Beamforming** Uniform linear S -channel digital array with analog to digital converters (ADCs) behind every antenna element. Each element is separated by $\frac{\lambda}{2}$. The incident wave has an angle of arrival of ϕ , resulting in a different time of flight for each antenna element.

In appended paper IV, the inference is wideband, and preferably adaptive wideband beamforming techniques should be applied. Adaptive wideband beamforming is outside the scope of the thesis but will be considered in future work. However, wideband interference will appear equivalent to several narrowband interfering signals

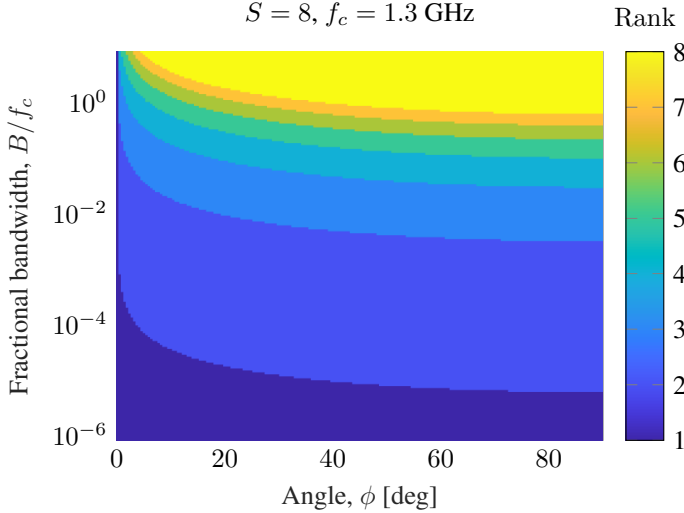


Figure 2.11: Rank of Adaptive Beamforming The rank of the covariance matrix required to suppress a wideband interfering signal when applying narrowband beamforming techniques such as the CAPON beamformer. The rank required depends on the fractional bandwidth (B/f_c), instantaneous SNR, number of antenna elements (S), and angle-of-arrival (ϕ).

from slightly different directions. Thus, given that the rank of the covariance matrix is sufficiently high, interfering signals can still be suppressed using narrowband techniques, but not as much as if applying wideband techniques. The angular suppression zone is also larger since signals appear to come from different directions. In Fig. 2.11, an example of the rank required to suppress a wideband signal is shown for various angles of arrivals and relative bandwidths. The example is for an antenna of $S = 8$ elements with a spacing of about 10 cm, and a carrier frequency of $f_c = 1.3$ GHz. The example parameters are the same as for the experimental setup in appended paper IV.

Although adaptive wideband beamforming is outside the scope of this thesis, a non-adaptive true time delay (TTD) beamformer is still implemented to steer the beam in different directions. Polynomial interpolation filters, specifically the Farrow filter structure, are implemented to achieve TTD efficiently. The Farrow filter structure of a cubic polynomial and its derivation is detailed in reference [108]. The benefits of Farrow filters are that the time delay is programmable by a single input parameter and that a limited amount of FPGA resources are required. The time delay suffers from a slight bias. However, the bias is deterministic and can thus be compensated for. The bias of a cubic (order 3) Farrow filter is seen in Fig. 2.12, where $\hat{\tau}$ is the resulting delay, and τ is the target delay. The bias error is often negligible.

Using the Farrow filters, the beam is steered by applying time delays for each channel, indexed by n , as

$$\tau_n = \frac{\lambda}{2c} n \sin(\phi). \quad (2.41)$$

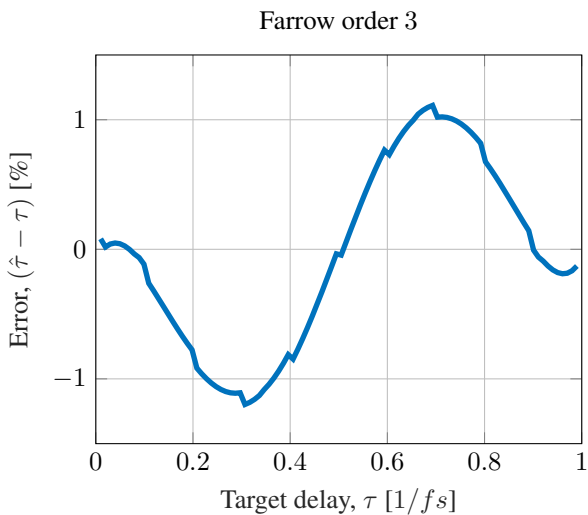


Figure 2.12: **Farrow Filter Delay Bias** Delay bias of a Farrow filter of order 3. The bias (or error) is the difference between the target delay τ and the resulting delay $\hat{\tau}$. The Farrow filter performs fractional resampling; thus, the x-axis is a fraction of the sampling interval.

Chapter 3

Hardware and Firmware Development

This chapter will present the hardware and firmware development. The appended paper I describes the construction of the transmitter. Section 3.1 serves to provide additional details, occasionally leading to some repetition. The transmitter has been continuously upgraded, and the version varies from experiment to experiment. However, the basic functionality is the same and only the final version is described. The real-time noise radar development is covered in appended paper III and IV. In appended paper III, the real-time processor operates in a monostatic mode, and in appended paper IV, it is upgraded to a bistatic mode. Section 3.2 will provide additional details about the real-time processor.

In appended paper I and II, data is directly streamed to disk drive storage for offline processing and analysis. A software-defined radio (SDR) is used as a receiver for those experiments. The SDR has a fixed sampling rate of 125 MS/s, requiring analog down-conversion before sampling. The setup is relatively simple but good enough for the tasks at hand. The receiver in appended paper III and IV is a microwave platform named the Vivace. In appended paper V, the receiver is an undisclosed digital receiver. Table 3.1 summarizes which transmitter and receiver are used for the experiments in the appended papers.

Table 3.1: List of the hardware utilized in the different experiments. See reference [109] and reference [110] for information about the Vivace and the SDR, respectively.

Appended Paper	I	II	III	IV	VI
Transmitter	Bistatic Tx	Vivace	Vivace	Bistatic Tx	Bistatic Tx
Receiver	SDR	SDR	Vivace	Vivace	Undisclosed Receiver



Figure 3.1: **Transmitter Unit** Picture of the L-band transmitter unit mounted underneath a hovering UAV. A schematic of the transmitter is shown in Fig. 3.2

3.1 Bistatic Transmitter

The design philosophy of the transmitter is that it should be flexible, lightweight, and easy to operate. It was initially constructed to operate in the L-band ($f_c = 1.3$ GHz) for several reasons: synergy with other Saab demonstrator platforms, reuse of specific components, like, the antenna elements, transmit license at several sites and direct sampling at the carrier frequency. However, it can operate up to about 6 GHz with relatively minor changes. For example, in appended paper V, it operates at a center frequency of 3.2 GHz. A brief transmitter description is also given in appended paper I. Here, however, a much more detailed description is given. Additionally, there have been upgrades since the publication of appended paper I.

The transmitter weighs about 4.2 kg, allowing it to be mounted underneath a DJI 600 Matrice unmanned aerial vehicle (UAV), as seen in Fig. 3.1. Note the rubber bands used for mounting, reducing high-frequency vibrations that were found to cause the waveform card to shut down. Although no measurements with a flying transmitter were performed within this thesis, it is planned for future work.

The transmitter components are assembled on printed circuit boards (PCBs). PCBs are relatively lightweight, robust, and rigid and allow for signal routing. In total, there are four PCB planes with different functions, divided into – going from top to bottom – the *Control Plane*, the *Waveform Generation Plane*, the *Power Amplification Plane*, and the bottom plane which is just for mounting and protection. The overall functionality of the different planes is illustrated in Fig. 3.2 and described below, starting with the *Waveform Generation Plane*.

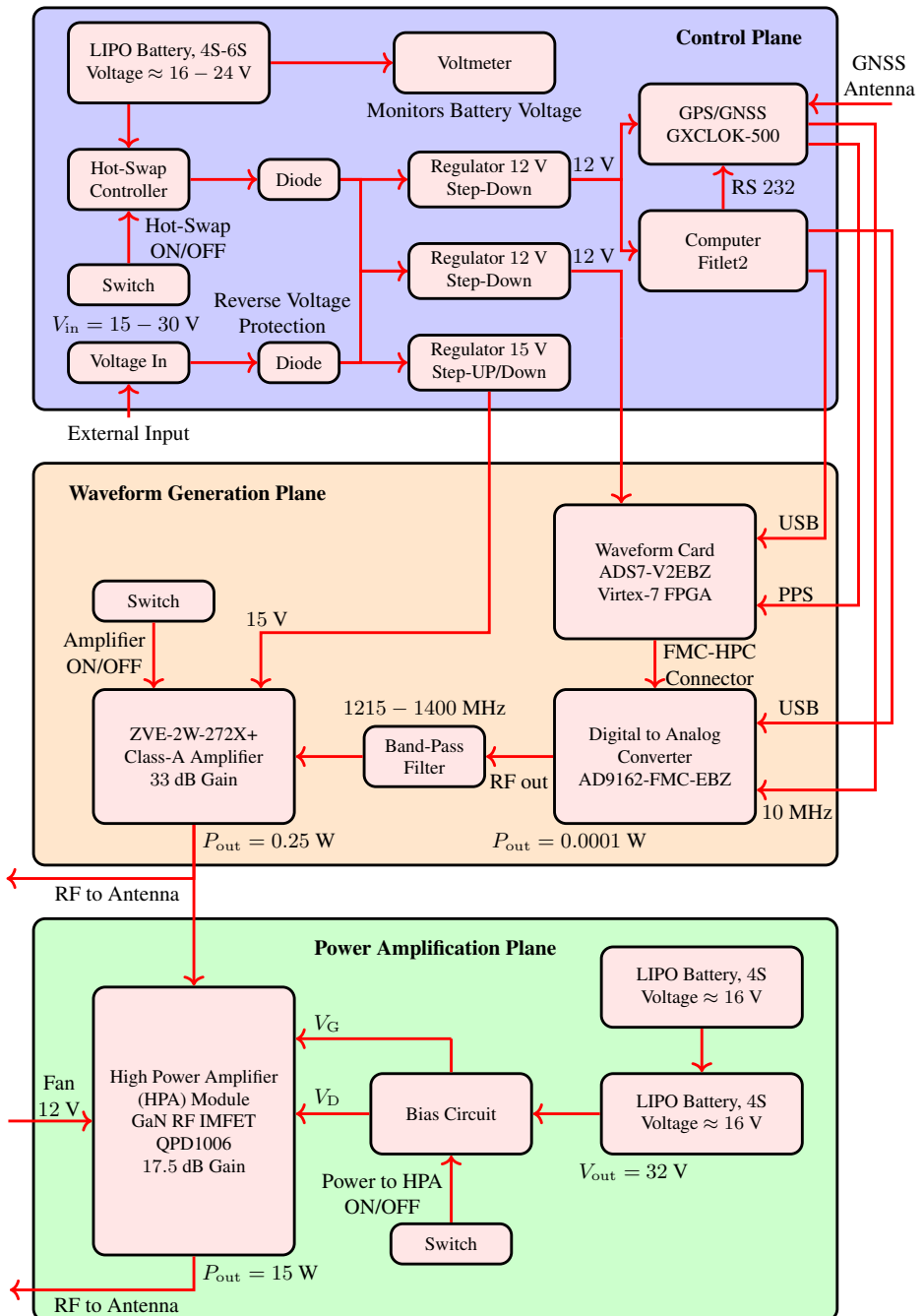


Figure 3.2: Transmitter Schematic The transmitter is divided into three planes, each with a specific function: the *Control Plane*, the *Waveform Generation Plane*, and the *Power Amplification Plane*. In summary, the *Waveform Generation Plane* generates the waveform – using a waveform card and a DAC – and performs analog filtering and amplification. The *Control Plane* controls the settings of the waveform generation through a mini-computer and maintains time and frequency synchronization using a GNSS unit. Additionally, all electronics are powered by an LIPO battery. The essential component of the *Power Amplification Plane* is a high power amplifier (HPA) module, further amplifying the signal, allowing for continuous transmission with an average output power of 15 W. Section 3.1 details each plane's specific functions.

3.1.1 Waveform Generation Plane

The *Waveform Generation Plane* is shown in Fig. 3.3. It utilizes the ADS7-V2 [111] evaluation board (waveform card) in combination with the AD9162-FMC-EBZ [112] digital-to-analog converter (DAC) to generate radio frequency (RF) signals. The waveform card is based on Xilinx's Virtex-7 FPGA. It has an accessible dynamic random-access memory (DRAM) of approximately 2 GB in which it is possible to download arbitrary waveforms, for example, noise waveforms created in Matlab. All waveforms are 16-bit IQ samples to allow for digital upconversion – 16-bits is the maximum bit depth of the DAC.

The waveforms are then read from the waveform card's memory and synthesized by the DAC. The DAC has a maximum sample rate of 12.6 GS/s, built-in digital up-conversion, and an interpolation filter with a maximum interpolation order of 24. To simplify the signal processing, it is convenient if the baseband sampling rates of the transmitter and receiver only differ by an integer factor. The receivers then constrict the transmitter's baseband sampling rate to 250 MS/s, which is achieved by setting the DAC sampling rate to 6 GS/s and the interpolation filter to 24. 250 MS/s refers to the complex sample rate and, thus, allows for transmitting waveforms with a maximum bandwidth of 250 MHz.

The synthesized signal is band-pass filtered and amplified by a class-A amplifier [113] with 33 dB gain and a maximum output of 2 W. The band-pass filter [114] has a pass band between 1215 - 1400 MHz, but the stop band of the filter is wide enough for the attenuation of waveforms with 250 MHz bandwidth to be negligible. Class-A amplifiers are the most linear, but they generally have low efficiency and output power. The output power of the DAC, for the specific amplitude-modulated noise waveforms considered, is approximately -9 dBm, resulting in an output power of about 24 dBm or 0.25 W after amplification. After amplification, the antenna transmits the signal, except for in appended paper IV. In appended paper IV, the signal is further amplified by a high-power amplifier module, described in Section 3.1.3.

In appended paper I, the class-A amplifier was characterized in terms of correlation losses as a function of input power. The results show that the behavior is relatively linear, even close to saturation. The definition of the correlation loss in appended paper I is unfortunately unclear, and a more precise formulation is given in (Eq. 3.1).

$$L_{\text{corr}} = \left| \frac{\max_k \left\{ \sum_n y_n x_{n-k}^* \right\}}{\sqrt{\sum_n |y_n|^2 \cdot \sum_n |x_n|^2}} \right|. \quad (3.1)$$

3.1.2 Control Plane

A picture of the *Control Plane* is shown in Fig. 3.4. A mini computer controls the settings of the waveform card and the DAC and downloads the waveforms to the waveform card's memory through universal serial bus (USB) communication. Settings include DAC sampling rate, interpolation, center frequency, frequency reference, and trigger options.

Maintaining synchronization in time and frequency is essential to distributed radar systems. Short-term stability is maintained by using high-quality local oscillators at each sub-system. To maintain long-term stability, navigation satellite system (GNSS)



Figure 3.3: Waveform Generation Plane A picture of the waveform generation plane described in Section 3.1.1. The plane consists of an FPGA, a DAC, a class-A amplifier, a band-pass filter (located underneath the DAC), and connectors and switches. The dimension of the PCB to which the components are mounted is 315×175 mm.

units [115] provide a 10 MHz GNSS disciplined frequency reference. The phase noise of the DAC and the 10 MHz global GNSS reference is shown in Fig. 3.5. The GNSS units also provide a pulse per second (PPS) output, which aligns the subsystems in time. The waveform card either transmits continuously – the card then deterministically loops the downloaded waveform – or it transmits when enabled by an analog logic signal. Each time the waveform card is enabled, the transmission restarts. Hence, the PPS enables transmission each second for as long as the PPS remains high. The mini-computer controls the time the PPS remains high and many other settings via recommended standard (RS) 232 communication.

All electronics are powered by batteries. The *Control Plane* and the *Waveform Generation Plane* are powered by a single 4S-6S lithium-ion polymer (LIPO) battery. The design allows batteries between 16 V and 30 V to be used. Step-down and step-up voltage regulators produce all necessary drive voltages. A voltmeter monitors the battery voltage to reduce the risk of depleting the battery beyond recovery – an improvement to this would be an automatic shutdown circuit.

A Hot-Swap controller circuit is implemented to connect or disconnect the battery safely. One of the main components of the Hot-Swap controller is an NPN transistor that is turned on or off by a manual switch to allow for safely connecting or disconnecting the battery. Additionally, the Hot-Swap controller limits inrush current and provides over-current protection. The transmitter operates for about 2 hours when powered by batteries, which is good enough for most field experiments but not good enough for lab testing. For lab testing, the transmitter is powered by a power supply. Thanks to the Hot-Swap controller and two diodes, the change from battery to power



Figure 3.4: Control Plane A picture of the control plane described in Section 3.1.2. The plane consists of a mini-computer, a LIPO battery, a GNSS unit, and various electronic components. The dimension of the PCB to which the components are mounted is 315×175 mm.

supply is performed seamlessly.

3.1.3 Power Amplification Plane

The *Power Amplification Plane* significantly increases the output power to achieve enhanced detection ranges – this is only utilized in appended paper IV as it is the only paper in which the CNF does not limit the detection sensitivity. Based on the data-sheet [116], the QPD1006 is very promising as a high-power amplifier. The maximum output power when transmitting the amplitude-modulated noise waveforms considered and when utilizing the class-A amplifier described in Section 3.1.1 as a drive amplifier is 15 W. With an output power of 15 W, the amplifier power consumption is about 50 W, that is, an efficiency of 30 %. Considering that the increase in the amplifier's chassis temperature is negligible, it should be able to handle higher dissipated energies without breaking. Thus, achieving higher output powers and efficiencies is possible by increasing the input power, which would require another drive amplifier. Further transmitter development is intended in future work.

The high-power module can be seen in appended paper IV (Fig. 2); it consists of the QPD1006 evaluation board mounted in an aluminum container, SMA contacts, and a central processing unit (CPU) fan on the back. The fan is powered by 12 V from the control plane, whereas the high power amplifier (HPA) is powered by two series-connected 4s LIPO batteries, providing about 32 V drain voltage (V_D). The drain voltage is backed off from the recommended 50 V to lower the overall dissipation.

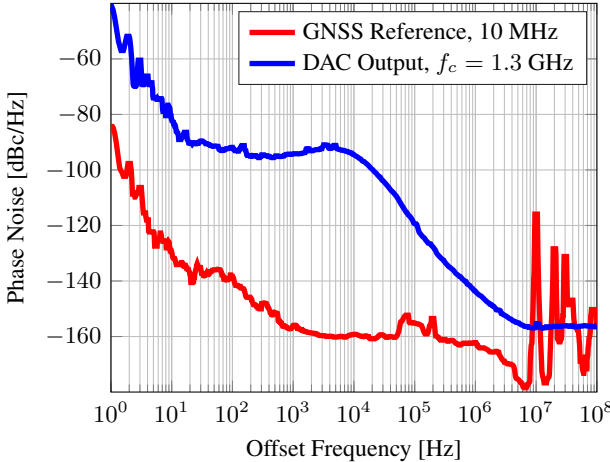


Figure 3.5: Phase Noise Measurement Phase noise measurement data from the 10 MHz GNSS reference and the DAC. The DAC is sampling with a rate of $f_r = 6$ GHz, at a carrier frequency of $f_c = 1.3$ GHz. The GNSS spurs at offset frequencies 10 MHz, 20 MHz, 30 MHz, etc., are intermodulation products of the center frequency.

The negative gate voltage (V_G) is generated by a voltage inverter mounted on the bias circuit. The bias circuit draws inspiration from an application note by Ampleon – see reference [117]. However, several additions and improvements have been implemented. Essential functions for this application include correct sequencing of applied V_D and V_G , Hot-Swap controller to allow for safe removal of the batteries, under-voltage protection, over current protection, limit inrush current, tunable V_G and maintaining stable V_G through a feedback loop. It also contains many other functions that are not necessary for this application.

The correlation losses in the signal processing due to non-linear effects in the HPA are not examined in the same detail as the class-A amplifier in appended paper I. They are only measured for the specific configuration used, in which the correlation losses are less than 0.5 dB. Higher correlation losses are expected if the output power is increased. To mitigate these losses, future work intends to study digital pre-distortion techniques [118].

The amplified RF signal is fed to a 4:1 power divider, splitting the signal to each of the four antenna elements. The antenna elements are configured in a 2×2 grid, resulting in a vertical and azimuth 3 dB beam width (Eq. (2.11)) of $0.88 \cdot 0.23 / 0.2 \approx 1$ rad or 60 degrees, in other words, a very wide lobe. The antenna elements have an approximated directivity of 5 dB. Thus, the total gain of the antenna is about 11.8 dB.

3.2 Vivace – Real-Time Noise Radar

The real-time noise radar is implemented on a digital microwave synthesis and analysis platform named Vivace [109], developed by *Intermodulation Products*. Vivace is based on the first generation Xilinx RFSoC hardware [119]. It comes with 8 DACs running

at up to 6.4 GS/s, 8 analog-to-digital converters (ADCs) running at up to 4 GS/s, low phase-noise clocking infrastructure, and significant FPGA, CPU and memory resources. The analog bandwidth of the inputs and outputs of the RFSoC and Vivace is high compared to the sampling rate. With proper reconstruction and anti-aliasing filters, signals in the second Nyquist zone can be directly synthesized and measured, enabling carrier frequencies up to 4 GHz. For more information about the platform and its use cases, see references [119, 120].

The functionality of the platform and the measurement core – referring to the radar-specific signal processing – is detailed in appended papers III and IV. This section will provide additional details and mention some improvements. The platform and the including analog electronics are seen in appended paper III (Fig. 5). For specifics relating to the required bit depth and the analog electronics, see appended paper III (Section 3.2.2 and Section 3.2.5).

A block diagram of the complete and finished noise radar model is shown in Fig. 3.6. The model is divided into five sub-functions: 1) *Signal Generation and Transmission*, 2) *Reception*, 3) *Fast Time Processing*, 4) *DRAM Operation*, 5) *Slow Time Processing and Data Readout*. Although the sampling rate varies, the clock rate is always 250 MS/s. The 3) *Fast Time Processing*, 4) *DRAM Operation* and 5) *Slow Time Processing and Data Readout* functionality is more or less the same as in appended paper III. The improvements are in 1) *Signal Generation and Transmission*, 2) *Reception*, and the surrounding control structure.

1) Signal Generation and Transmission: The FIR filter now features more taps, precisely 201 complex coefficients, allowing the system to operate with a broader range of bandwidths. It is also now possible to change the coefficients between each startup. Arbitrarily, the spectrum is acceptable down to about 3 MHz. Furthermore, D – the downsampling parameter – can now be any 2 exponent where $D = 64$ would result in a baseband sampling rate of 3.9 MHz, which is suitable if operating with 3 MHz bandwidth. The noise radar is thus no longer limited by the modes described in appended paper III (Table. 1).

Considering that 201 complex coefficients require 402 digital signal processor (DSP) resource blocks, the noise filter makes up 10 % of the available DSP resources.

2) Reception The receiver now utilizes all of Vivace's 8 available channels to apply beamforming. The beamforming portion is detailed in appended paper IV. After the beamforming, the signal is FIR-filtered to avoid aliasing when downsampled by a factor of 2. The second FIR filter uses the same taps as the noise filter in 1) *Signal Generation and Transmission*, which is an improvement from previous implementations. Without the second FIR filter, the noise figure is increased. Previously, in appended paper III, when mainly operating with 200 MHz bandwidth, the increase in noise figure is negligible, but if operating with 3 MHz, the second FIR filter is essential.

Other improvements in control structure include frequency synchronization on external GNSS reference, LFSR generators that can reset on external triggers, and the ability to switch between monostatic and bistatic operation.

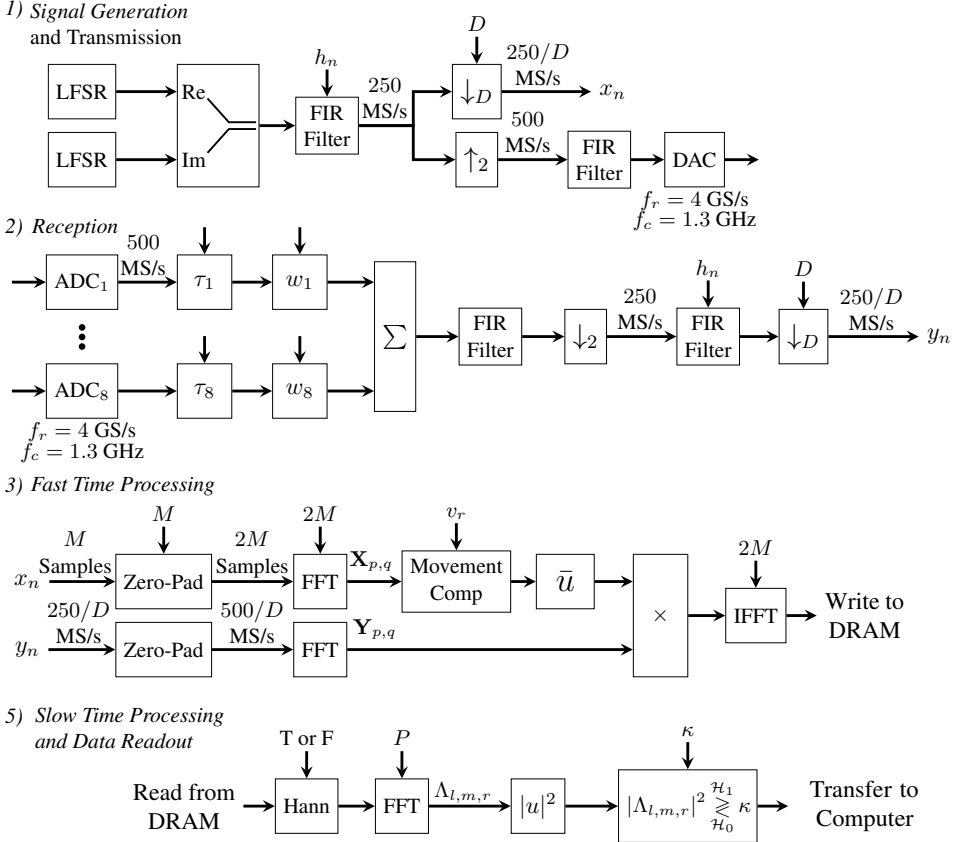


Figure 3.6: **Receiver Schematic** The digital real-time receiver is divided into 5 different functions, each one is described in detail in appended paper III and IV and important changes are covered in Section 3.2. Boxes with arrows entering at the top indicate that the parameter is configurable.

3.2.1 Offline Data Collection

Vivace also has an offline data collection mode. The received signal is digitally downconverted to the baseband and downsampled to a sampling rate of 62.5MS/s. It is then saved to DRAM before being read out to Matlab. The bit depth is 32-bits (16-bits I and 16-bits Q), resulting in a total data rate of 2 GB/s. The DRAM that performs the intermediate storage has a memory size of about 2 GB; thus, it is possible to save roughly 1 s of data for offline analysis. Higher bandwidths would require higher data rates, which are not supported by the DRAM.

The offline data collection is used for calibrating the system, calculating the beamforming covariance matrix (see appended paper IV), and gathering offline data for detailed analysis. Future experiments aim to use the offline data collection for bistatic multiple-input and multiple-output (MIMO) experiments when a multi-channel transmitter has been developed.

3.2.2 Matlab User Interface

The real-time processor is controlled from Matlab. Data processed by the FPGA is transferred directly to a computer via Ethernet. The computer collects the data and plots a range-Doppler map.

Most model parameters are configurable, and many are even run-time configurable. The FPGA core must be rebooted to change the non-run-time configurable parameters, which only takes about 1s. The system is highly configurable and an excellent demonstrator platform. The functionality of the real-time processor allows for changing integration times and bandwidth, performing both narrowband and wide-band beamforming, moving target compensation, switching between monostatic and bistatic operation, adaptive thresholding, etc. Even an ad-hoc tracking filter is currently implemented in Matlab, but this could be improved to something more advanced. Additionally, the platform can operate at any frequency up to 4 GHz by changing the analog electronic components.

The platform has all the necessary functionality to operate as a short-range surveillance radar. However, it would require an improved Matlab control structure, which is outside the scope of this thesis. Future work will improve the Matlab control structure. Even without an improved control structure, a technology readiness level (TRL) of 7 has been achieved.

3.2.3 FPGA Resource Utilization

The final resource utilization of the FPGA platform is seen in Fig. 3.7. Critical resources such as DSPs and block random access memory (BRAMs) are close to the maximum, limiting the implementation of further functionality. Although it is possible for some optimizations, discussed in appended paper III, it highlights the complexity of operating high time-bandwidth noise radars, especially as the current implementation only performs one velocity hypothesis and no parallel beamforming, acceleration hypothesis, or clutter filtering.

3.2.4 Calibration

The platform and the accompanying analog electronics are calibrated in terms of amplitude, phase, and time delay. One specific problem with the Vivace is that the internal microstrip is not of even length, thus requiring true time delay (TDD) compensation.

The analog electronics is calibrated using a vector network analyzer (VNA), but a VNA measurement cannot calibrate the Vivace. Calibrating the amplitude is simple – take the root mean square average of any signal – but the phase difference and time delay are more challenging. The ZCU111 Xilinx FPGA comes with multi-tile synchronization [121], guaranteeing that the ADCs are in phase. However, it is preferable to verify this.

Phase and time delay is calibrated using two sine signals of different frequencies. The phase delay τ_Φ is defined as

$$\tau_\Phi = -\frac{\Phi}{2\pi f_c}, \quad (3.2)$$

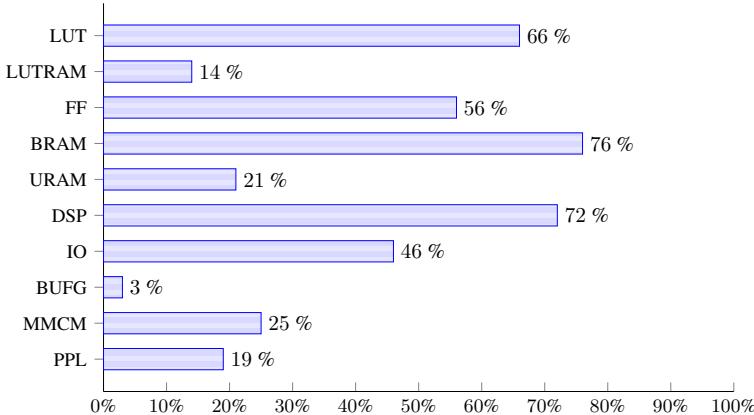


Figure 3.7: FPGA Resource Utilization FPGA resources utilized by the final implementation. These resources include look-up table (LUT), look-up table random access memory (LUTRAM), flip flops (FF) block random access memory (BRAM), ultra random access memory (URAM), digital signal processor (DSP), inputs and outputs (IO), global clock buffer (BUFG), mixed-mode clock manager (MMCM) and phase-locked loop (PLL)

Table 3.2: Relativ time delays between different channels in the Vivace caused by different lengths on the microstrip.

Channel	1	2	3	4	5	6	7	8
Time Delay [ns]	0.70	0.68	0.63	0.60	0.01	0	0.2	0.17

where Φ is the phase shift. If the ADCs are in phase, the phase-delay should be equal for the two frequencies. Performing the measurement, it was verified that the ADCs were in phase, and the time difference between each channel was calculated to the values in table 3.2. The TTD is performed during real-time operation using the implemented Farrow filter structure.

Chapter 4

Results

The appended papers present the relevant measurements and results. This chapter gives more context to some of those results and summarizes the main findings in the papers. In Section 4.1 Sequential-CLEAN’s superior performance compared to the CLEAN and Lattice filter algorithms is shown. Next, additional adaptive beamforming results are shown in Section 4.2. The main findings of each paper are summarized in Section 4.3.

4.1 CLEAN and Lattice Filter

Fig. 4.1 shows the results without clutter suppression and with clutter suppression when applying the CLEAN and lattice filter algorithms for the monostatic and bistatic setup considered in appended paper I. These results should be compared with the results of the sequential CLEAN algorithm shown in appended paper I (Fig. 9).

All algorithms perform well and have similar performance in the bistatic setup. The clutter environment in the bistatic setup is much simpler than the monostatic setup – there is less strong and distributed clutter present – which is likely why all algorithms perform well.

In the monostatic setup, the lattice filter performs the worst. Still, the CLEAN and sequential CLEAN have similar performance, but the sequential CLEAN algorithm is slightly better. Since CLEAN and sequential CLEAN are very similar, improvements in the sequential CLEAN algorithm are, in many instances, also applicable to the CLEAN algorithm. In Fig. 4.1 these improvements are applied to the CLEAN implementation, hence the performance between CLEAN and sequential CLEAN is more similar than it was in the writing of appended paper I.

The results vary slightly depending on the parameter settings, and it is unclear how to conduct a fair comparison between the algorithms. For example, should aspects such as calculation times be factored in the comparison? If so, the implementations must be optimal, which they are not. Regardless, the ECA implementation in paper VI is superior, and continued work will focus on improving that implementation.

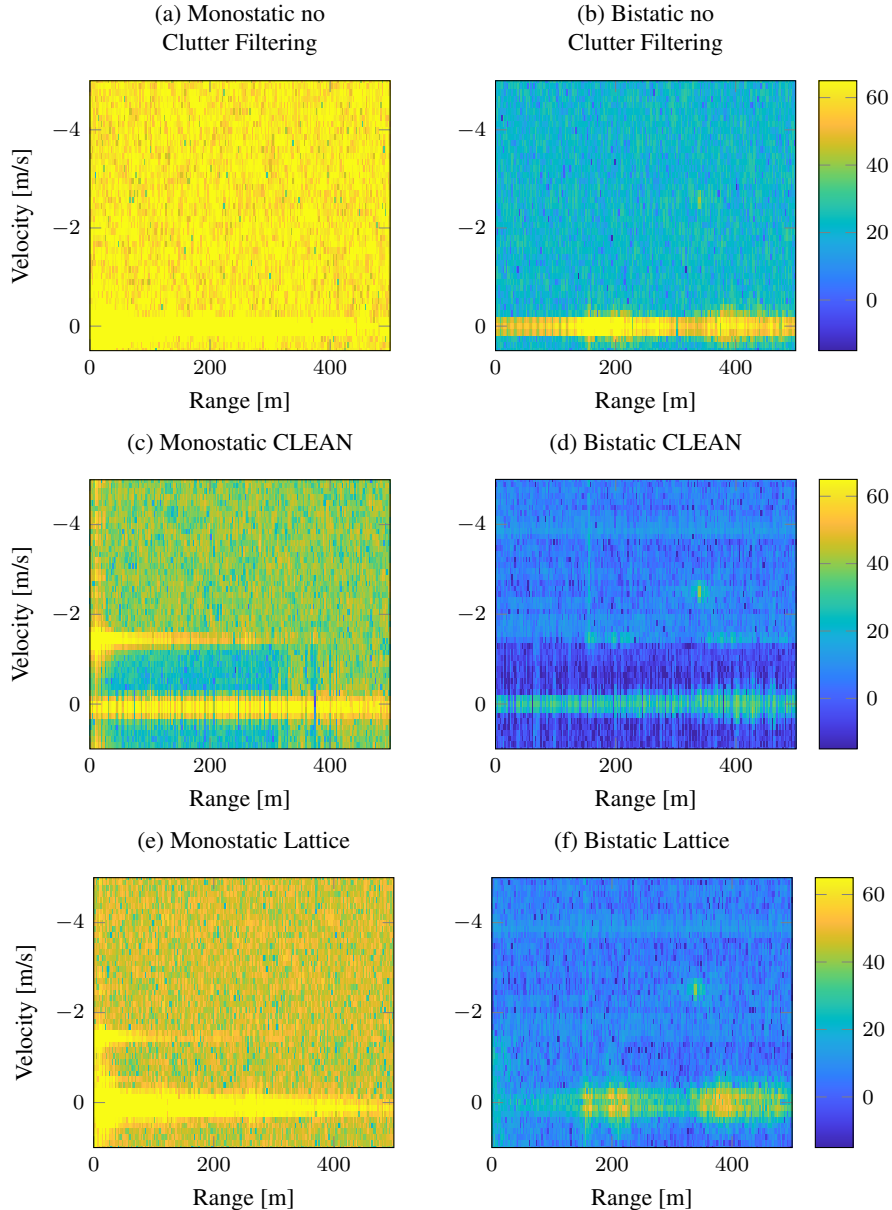


Figure 4.1: Results without clutter reduction and with clutter reduction for the CLEAN and Lattice filter algorithms described in Section 2.2.7. The results should be compared to those in appended paper I (Fig. 9). In the bistatic setup, all algorithms perform fairly well, but the sequential CLEAN algorithm performs best in the monostatic setup's more complicated clutter environment.

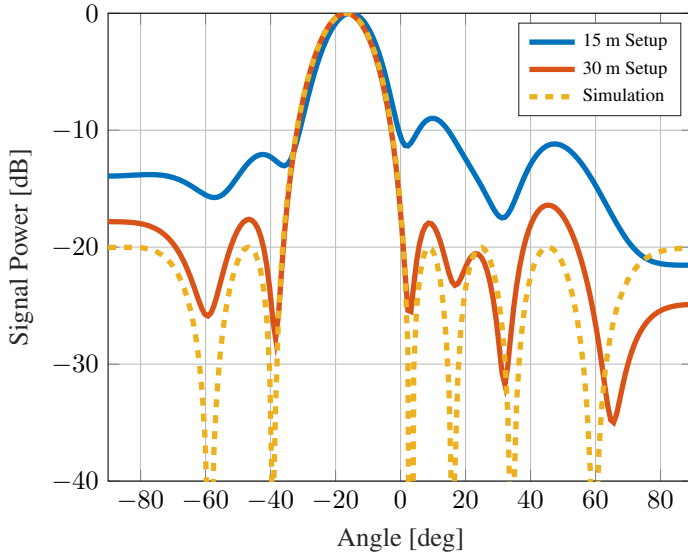


Figure 4.2: Power as function of angle for the 30 m setup, the 15 m setup and for simulation data. The results from the 30 m setup coincide well with the simulation data, indicating that only one dominant interfering signal is present. In the 15 m setup, the power is more distributed over angle, indicating wideband effects.

4.2 Adaptive Beamforming

In appended paper IV, the improvement in detection sensitivity due to adaptive beamforming is clearly illustrated in Fig. 3. As stated in the paper, two different measurement setups were tested, one with 30 m separation between the transmitter and receiver, and another with 15 m separation. In the paper, only the results for 30 m setup is shown as results for the 15 m setup was not particularly good. The reason for that is wideband effects.

In Fig. 4.2, the measured power as a function of an angle is shown for the 30 m setup, the 15 m setup, and for simulated data containing one wideband interfering signal. The 30 m setup results coincide well with the simulation, indicating that there is one dominant narrowband interfering signal present, which the CAPON beamformer effectively suppresses. For the 15 m results, the measured power is more distributed over all angles, indicating wideband effects which limits the effectiveness of beamforming. Future work will investigate the Frost beamformer [122].

However, wideband effects are most prominent when the separation between the transmitter and receiver is small. In a proper bistatic system, the separation is large and then wideband effects are less of an issue.

4.3 Paper Summaries and Main Findings

The appended papers are summarized below.

I Noise Radar: Demonstration of Correlation Noise Suppression

In the appended paper, bistatic operation is considered a solution to reduce the CNF in noise radar systems. To demonstrate the advantage of bistatic operation compared to monostatic operation, a bistatic noise radar system was constructed. Emphasis was put on developing a flexible and lightweight transmitter that can be mounted on a commercial UAV, whereas the receiver was a commercial off-the-shelf software-defined radio.

The transmitter allows for predefined waveforms created in, for example, Matlab to be downloaded to the transmitter's DRAM. Thus, the transmitter can transmit completely arbitrary waveforms. The DRAM has an accessible memory size of 2 GB, enabling transmission of a high-bandwidth signal for over several seconds. The transmitter weighs roughly 4.2 kg and has a maximum output power of 2 W. All the electronics are battery-powered, and continuous operation can be sustained up to 1 h.

The bistatic system uses pseudo-random noise generated locally at the receiver and transmitter units. The two subsystems do not communicate directly. Instead, the seed of the pseudo-random generator is agreed upon beforehand. Transmission and reception are triggered by a pulse per second from GNSS units, which also maintain frequency synchronization. Correlation losses due to nonlinearities in the transmitter and receiver units were measured to 0.1 dB.

In the experiments, the transmitter and receiver are separated by approximately 400 m, which reduces the CNF by 40 dB compared to the monostatic setup (roughly 1.5 m separation between the receiver and transmitter antenna). Larger separations will improve the CNF suppression. The bistatic system was shown to detect a slow-flying UAV at a range of 400 m with a signal-to-interference-plus-noise ratio (SINR) of about 21 dB. However, the detection performance is still limited by the CNF.

A CLEAN algorithm was implemented to further suppress the CNF. In the monostatic and bistatic setups, respectively, an additional suppression of 23 dB and 19 dB was achieved. The detection sensitivity in the bistatic setup is then limited by thermal noise and not by clutter; therefore, the suppression is less than that of the monostatic setup. With 19 dB additional suppression of the CNF and assuming a detection threshold of 13 dB, the system should be capable of detecting the UAV at a distance up to 1900 m. However, that was not demonstrated.

The paper's primary conclusion is that bistatic separation should be considered a practical tool to reduce the masking effect. Bistatic operation also has many other advantages, which are discussed in the appended papers. Additionally, the work resulted in a capable bistatic transmitter that was and will be used for many future experiments.

II Experimental Evaluation of Moving Target Compensation in High Time-Bandwidth Noise Radar

This paper mainly investigated an algorithm to compensate for range-walk and Doppler spread. Compensation is crucial if operating with large bandwidth and/or long integration time to mitigate SINR losses. The algorithm implemented is a known algorithm suitable for batched processing and real-time implementation. However, experimental verification was lacking. Additionally, the paper examined the low Doppler tolerance of noise waveforms and the coherence time limit of small UAVs.

The algorithm's performance was studied using pseudorandom noise, with a bandwidth of 100 MHz. A UAV flying at a speed of 11.5 m/s was used as a target. Integrating for 1 s without range-walk and Doppler spread compensation would result in a loss of about 18.7 dB. By applying range-walk and Doppler spread compensation, the SINR improvement was about 18 dB, demonstrating the algorithm's effectiveness. Applying Doppler compensation to account for the waveform's low Doppler tolerance further increased the SINR by around 2 dB.

Knowing that the range-walk and Doppler spread compensation algorithm is successful, the maximum coherent integration time of the UAV was investigated. From the data, it is difficult to draw a firm conclusion. However, it was shown that the coherent integration time can be as large as 2.5 s.

The paper's main findings are that range-walk, and Doppler spread compensation are highly successful and that long integration times can be achieved on relatively small UAVs. Additionally, the results from this paper and appended paper I gave enough confidence to start working on a real-time noise radar implementation, see appended paper III.

III Implementation of a Coherent Real-Time Noise Radar System

The paper details the implementation of a continuous real-time monostatic noise radar system on an FPGA. Constructing prototypes is an essential step toward realizing commercial noise radar systems. With the development of digital electronics, it is now possible to implement real-time and continuous noise radar systems operating with a high time-bandwidth product, which this paper demonstrates.

The constructed system can operate with 100 % duty cycle, 200 MHz bandwidth, and 268 ms integration time while processing a range of about 8.5 km. Additionally, the system performs real-time moving target compensation to reduce range-walk and Doppler spread. The system operates with a digital reference signal generated in real-time by LFSRs. System performance is primarily limited by the memory bandwidth of the off-chip dynamic random access memory (DRAM). Higher bandwidths, for example, would be possible with higher memory bandwidths. A video of the system in action, demonstrating the real-time detection of a UAV, can be seen in reference [83]. The difference between applying range-walk and Doppler spread compensation and not doing so is also clearly illustrated. The CNF limits the detection range to about 100 m.

The main results of the work presented in the paper are (1) digital electronics have advanced to the point that it is possible to construct real-time noise radar systems and (2) the construction of a real-time noise radar demonstrator.

IV Real-Time Bistatic Noise Radar with Adaptive Beamforming

The work performed in appended paper I and appended paper III resulted in a capable bistatic transmitter and real-time monostatic noise radar. With minor changes of the two subsystems, a real-time bistatic noise radar system is realized.

The transmitter described in appended paper I is improved by including an HPA that can output 15 W continuously. Several minor changes are made to the receiver described in appended paper III to allow for bistatic reception. The only major change is the inclusion of several receiver channels to enable adaptive beamforming. In total, 8

receiver channels in a horizontal fully digital uniform linear array (ULA) configuration are used.

Adaptive beamforming is applied to suppress self-interference. Strong self-interfering signals, such as the direct signal, are treated in the same way as an interfering signal originating from a jammer. Initial offline experiments demonstrate the effectiveness of applying adaptive beamforming to suppress the direct signal and, thereby, the CNF. For the setup demonstrated, a suppression of more than 12 dB is achieved. The initial experiments verified that the signal processing works as expected before performing the real-time demonstration. Not much care should be given to 12 dB improvement since this depends on several factors. For more information, see the paper.

The bistatic real-time demonstration – the conclusion of the PhD – showcases the detection of a UAV at a range of more than 3.2 km, a substantial improvement compared to the detection range of 100 m in appended paper III. A video of the demonstration can be seen in reference [83]. The system's detection sensitivity is limited by thermal noise, not self-interference. Hence, much greater detection ranges could be achieved by increasing the output power. Since self-interference was not limiting, there was no benefit in applying adaptive beamforming.

This paper signified the end of the PhD. Referring to the goal in section 1.4, it should be considered a success. The results are a real-time bistatic noise radar system, complete with both narrowband and wideband adaptive beamforming, range-walk and Doppler spread compensation, adjustable bandwidth, integration times and PRFs, CFAR detection, and more. Matlab controls the system, and by further developing the control script, everything above could be adaptive. The functionality included in the FPGA makes it a very versatile demonstrator, and in my opinion, it is the world's foremost noise radar system.

V Aspects of Operating Low-Cost Bistatic Radar Transmitters

The final paper considers different aspects of operating low-cost bistatic transmitters. It is not a paper about noise radars; it is a paper about bistatic range-Doppler radar. However, the results and the discussion are highly relevant for noise radar implementations as well. The paper is based on work performed in the service for Saab, and therefore, some data is anonymized.

One of the major advantages of bistatic operation is that the receiver is silent and, thereby, undetected. However, the transmitter is still at risk, and it is desirable that it be low-cost so it is expendable to a certain degree. Low-cost transmitters come with design trade-offs, such as low gain. Low gain transmitters are favorable since pulse chasing is avoided, but the SNR is reduced if not compensated for.

Digital radars can simultaneously observe a large volume through parallel digital beamforming. Thus, increased integration times can compensate for lower gain. Increasing the integration time results in various effects, such as range-walk, Doppler spread, and target decoherence. All of these effects are also problematic for noise radar operations.

The paper describes the construction of a low-cost, compact, but powerful transmitter unit. The receiver used is fully digital. Using commercial airplanes as targets, all of the above-mentioned effects are observed, and various methods are successfully

applied to manage these effects.

The conclusion is that operating with high time-bandwidth products is, in principle, possible, but it is one thing to compensate for various effects on specific datasets, implementing a systematic real-time approach is something completely different. The latter requires significant work. The construction of the transmitter is also an important step towards increasing the technology readiness level of bistatic systems.

Chapter 5

Conclusions and Outlook

The thesis focused on developing and demonstrating a functional noise radar system with acceptable performance. That has been achieved; the platform's functionality is such that, with an improved control interface, it could be deployed as a short-range air surveillance radar against slow-moving targets. Thus, a technology readiness level of seven has been reached. With some improvements and a more thought-out way of operation, arbitrary waveform radar could be ready for commercial implementation within a few years. However, the critical question is: Are the potential use cases strong enough to motivate arbitrary waveforms?

Achieving a high level of LPI is extremely difficult. One-way propagation versus two-way propagation will always be a reality, and the required time-bandwidth product to mitigate that is likely not feasible as of now. Future improvements in processing power and algorithm development may enable very high time-bandwidth radar operation, but as discussed in append paper III, Moore's law might no longer hold.

Of course, transmitting a waveform with no range and Doppler ambiguities is interesting, but other methods exist to resolve these issues. The same applies to low mutual interference; there are other solutions to the problem. LPE and LPID performance still applies, although transmission within a radar frequency band will imply that the transmission is from a radar. As stated in the Introduction, I am primarily interested in the ability to operate with arbitrary waveforms, rather than noise. Such abilities can enable a higher level of spectrum sharing, allowing radars access to the telecommunications band and vice versa. It might enable the reuse of existing telecommunication hardware for radar purposes, dramatically reducing the cost of radar production. Joint communication and sensing (JCAS) is currently a very active research field [123–125], but what it will lead to is uncertain. Changes in legislation regarding the allocation of frequency bands are likely determined by the big corporations and not by researchers.

If LPI aspects are less important, the time-bandwidth product can be kept at reasonable limits, for example, 50 dB. Arbitrary waveform operation is then significantly simplified; the requirements on moving target compensation and acceleration are relaxed,

and fewer computational resources are required. With lower time-bandwidth products, the technology required to implement a radar operating with arbitrary waveforms is mature enough. A lower time-bandwidth product decreases the CNF suppression, but the suppression should still be sufficient with a bistatic setup and adaptive beamforming. The possibility of applying clutter reduction algorithms also exists in very difficult clutter situations.

Continued research will investigate transmitter architecture, focusing on maximum average power and efficiencies for CW amplifiers when transmitting arbitrary waveforms. Forcing the amplifier into the non-linear regime increases the possibility of unwanted modulations, which can result in a correlation loss. Applying digital predistortion might reduce the correlation loss and enable higher output power [126] – this will be investigated. Future research will also improve the ECA algorithm implemented in paper VI to make it more computationally effective, and adaptive broadband beamforming will be further investigated.

A dedicated noise radar receiver will likely utilize a mix of graphics processing units (GPUs), FPGAs, and CPUs hardware. Finding a suitable hardware mix and resource allocation would be very interesting. However, as stated, I see arbitrary waveform operation as a complement to monostatic pulse-Doppler operation, and then the receiving hardware is constrained by the already in-use monostatic platform. That is one of many reasons why processing arbitrary waveforms similarly to pulse-Doppler radar processing is preferred. Future internal work at Saab will investigate how to best implement arbitrary waveform modes in current and future products. Operating with arbitrary waveforms is possible in the coming years, but its applications are less certain.

Bibliography

- [1] B. M. Horton, “Noise-modulated distance measuring systems,” *Proceedings of the IRE*, vol. 47, pp. 821–828, 1959.
- [2] R. Narayanan, “Noise radar techniques and progress,” in *Advanced Ultrawideband Radar: Signals, Targets, and Applications*, J. Taylor, Ed. CRC Press, 2016, pp. 323–361.
- [3] R. M. Narayanan, Y. Xu, P. D. Hoffmeyer, and J. O. Curtis, “Design, performance, and applications of a coherent ultra-wideband random noise radar,” *Optical engineering*, vol. 37, pp. 1855–1869, 1998.
- [4] S. R. J. Axelsson, “Analysis of random step frequency radar and comparison with experiments,” *IEEE Transactions on Geoscience and Remote Sensing*, vol. 45, pp. 890–904, 2007.
- [5] P. E. Pace, *Detecting and classifying low probability of intercept radar*, 2nd ed. Artech house, 2009.
- [6] F. D. Palo, G. Galati, G. Pavan, C. Wasserzier, and K. Savci, “Introduction to noise radar and its waveforms,” *Sensors*, vol. 20, 2020.
- [7] G. Galati and G. Pavan, “Measuring the anti-intercept features of noise radar waveforms: the way ahead,” in *2022 IEEE 9th International Workshop on Metrology for AeroSpace (MetroAeroSpace)*, 2022, pp. 174–178.
- [8] G. Galati, G. Pavan, and C. Wasserzier, “Interception of continuous-emission noise radars transmitting different waveform configurations,” in *2022 23rd International Radar Symposium (IRS)*, 2022, pp. 153–158.
- [9] M. Heino, J. Marin, K. Hiltunen, M. Turunen, and T. Riihonen, “Theoretical and experimental analysis of the supposed stealthiness of noise radar,” in *2023 IEEE Radar Conference (RadarConf23)*, 2023, pp. 1–6.
- [10] G. Galati, G. Pavan, K. Savci, and C. Wasserzier, “Counter-interception and counter-exploitation features of noise radar technology,” *Remote Sensing*, vol. 13, 2021.

- [11] T. Thayaparan and C. Wernik, “Noise radar technology basics,” Defence R&D Canada, Tech. Rep., 2006.
- [12] T. Thayaparan, M. Daković, and L. Stanković, “Mutual interference and low probability of interception capabilities of noise radar,” *IET Radar, Sonar & Navigation*, vol. 2, pp. 294–305, 2008.
- [13] M. Dawood and R. M. Narayanan, “Generalised wideband ambiguity function of a coherent ultrawideband random noise radar,” *IEE Proceedings - Radar, Sonar, and Navigation*, vol. 150, pp. 379–386, 2003.
- [14] S. R. J. Axelsson, “Noise radar using random phase and frequency modulation,” *IEEE Transactions on Geoscience and Remote Sensing*, vol. 42, pp. 2370 – 2384, 2004.
- [15] ——, “Suppression of noise floor and dominant reflectors in random noise radar,” in *2006 International Radar Symposium*, 2006, pp. 1–4.
- [16] K. Savci, A. G. Stove, F. De Palo, A. Y. Erdogan, G. Galati, K. A. Lukin, S. Lukin, P. Marques, G. Pavan, and C. Wasserzier, “Noise radar—overview and recent developments,” *IEEE Aerospace and Electronic Systems Magazine*, vol. 35, pp. 8–20, 2020.
- [17] K. S. Kulpa and Z. CzeKała, “Masking effect and its removal in PCL radar,” *IEE Proceedings, Radar, Sonar and Navigation*, vol. 3, pp. 174–178, 2005.
- [18] B. Stec and W. Susek, “Theory and measurement of signal-to-noise ratio in continuous-wave noise radar,” *Sensors*, vol. 18, 2018.
- [19] A. Popov, P. Rybkin, and V. Vasil’ev, “The report of experiments on electrical wireless signalization performed by a mine detachment during the campaign of 1897,” collection of documents and materials 50 Years of Radio. Invention of Radio by A.S. Popov, ed. by A.I. Berg, Academy of Science Publishing House, 1945 (in Russian).
- [20] “Das Telemobiloskop von Christian Hülsmeyer, Düsseldorf,” Deutsche Patentschrift Nr. 165546 30.04.1904.
- [21] R. C. Watson, *Radar Origins Worldwide: History of Its Evolution in 13 Nations Through World War II*. Trafford Publishing, 2009.
- [22] R. Bourret, “A proposed technique for the improvement of range determination with noise radar,” *PROCEEDINGS OF THE INSTITUTE OF RADIO ENGINEERS*, vol. 45, pp. 1744–1744, 1957.
- [23] G. Turin, “Comments on ‘a proposed technique for the improvement of range determination’,” *Proceedings of the IRE*, vol. 46, pp. 1757–1758, 1958.
- [24] H. Hochstadt, “Comments on ‘a proposed technique for the improvement of range determination’,” *Proceedings of the IRE*, vol. 46, p. 1652, 1958.

- [25] S. E. Craig, W. Fishbein, and O. E. Rittenbach, “Continuous-wave radar with high range resolution and unambiguous velocity determination,” *IRE Transactions on Military Electronics*, vol. MIL-6, pp. 153–161, 1962.
- [26] M. Carpentier, “Using random functions in radar applications,” *De Ingenieur*, vol. 82, pp. 166–172, 1970.
- [27] R. B. Chadwick and G. R. Cooper, “Measurement of ocean wave heights with the random-signal radar,” *IEEE Transactions on Geoscience Electronics*, vol. 9, pp. 216–221, 1971.
- [28] J. Smit and W. Kneefel, “RUDAR-an experimental noise radar system,” *De Ingenieur*, vol. 83, pp. 99–110, 1971.
- [29] R. B. Chadwick, “Measurement of distributed targets with the random signal radar,” *IEEE Transactions on Aerospace and Electronic Systems*, vol. AES-8, pp. 743–750, 1972.
- [30] J. Forrest and J. Meeson, “Solid-state microwave noise radar,” *Electronics Letters*, vol. 12, pp. 365–366, 1976.
- [31] J. Forrest and D. Price, “Digital correlation for noise radar systems,” *Electronics Letters*, vol. 14, p. 581–582, 1978.
- [32] R. M. Narayanan and M. Dawood, “Doppler estimation using a coherent ultrawide-band random noise radar,” *IEEE Transactions on Antennas and Propagation*, vol. 48, pp. 868–878, 2000.
- [33] S. R. J. Axelsson, “Noise radar for range/Doppler processing and digital beam-forming using low-bit ADC,” *IEEE Transactions on Geoscience and Remote Sensing*, vol. 41, pp. 2703–2720, 2003.
- [34] G.-S. Liu, H. Gu, W.-M. Su, H.-B. Sun, and J.-H. Zhang, “Random signal radar - a winner in both the military and civilian operating environments,” *IEEE Transactions on Aerospace and Electronic Systems*, vol. 39, pp. 489–498, 2003.
- [35] K. S. Kulpa, *Signal processing in noise waveform radar*. Artech House, 2013.
- [36] D. Bok, D. O’Hagan, and P. Knott, “Effects of movement for high time-bandwidths in batched pulse compression range-Doppler radar,” *Sensors*, vol. 21, 2021.
- [37] R. M. Narayanan, “Through-wall radar imaging using UWB noise waveforms,” *Journal of the Franklin Institute*, vol. 345, pp. 659–678, 2008.
- [38] K. Lukin, A. Mogyla, V. Palamarchuk, P. Vyplavin, O. Zemlyaniy, Y. Shiyan, and M. Zaets, “Ka-band bistatic ground-based noise waveform SAR for short-range applications,” *IET Radar, Sonar & Navigation*, vol. 2, p. 233 – 243, 2008.
- [39] P.-H. Chen, M. C. Shastry, C.-P. Lai, and R. M. Narayanan, “A portable real-time digital noise radar system for through-the-wall imaging,” *IEEE Transactions on Geoscience and Remote Sensing*, vol. 50, pp. 4123–4134, 2012.

- [40] M. Malanowski and K. S. Kulpa, “Detection of moving targets with continuous-wave noise radar: Theory and measurements,” *IEEE Transactions on Geoscience and Remote Sensing*, vol. 50, pp. 3502–3509, 2012.
- [41] W. Susek and B. Stec, “Through-the-wall detection of human activities using a noise radar with microwave quadrature correlator,” *IEEE Transactions on Aerospace and Electronic Systems*, vol. 51, pp. 759–764, 2015.
- [42] K. Savci, A. Y. Erdogan, and T. O. Gulum, “Software defined L-band noise radar demonstrator,” in *2016 17th International Radar Symposium (IRS)*, 2016, pp. 1–4.
- [43] K. A. Lukin, O. V. Zemlyaniy, D. N. Tatyanko, S. Lukin, and V. Pascazio, “Noise radar design based on fpga technology: On-board digital waveform generation and real-time correlation processing,” in *2017 18th International Radar Symposium (IRS)*, 2017, pp. 1–7.
- [44] E. Shareef, M. Dawood, and J. Boehm, “Experimental results to reduce side-lobes in random noise and linear frequency modulated signals,” *Electronics Letters*, vol. 53, pp. 564–566, 2017.
- [45] W. Susek, M. Knioła, and B. Stec, “Buried objects detection using noise radar,” in *2018 22nd International Microwave and Radar Conference (MIKON)*, 2018, pp. 461–463.
- [46] C. Wasserzier, A. G. Stove, and K. A. Lukin, “Verification of a continuous wave noise radar,” in *20th International Radar Symposium (IRS 2019)*, 2019, pp. 1–10.
- [47] K. Savci, A. G. Stove, A. Y. Erdogan, G. Galati, K. A. Lukin, G. Pavan, and C. Wasserzier, “Trials of a noise-modulated radar demonstrator – first results in a marine environment,” in *20th International Radar Symposium (IRS 2019)*, 2019, pp. 1–9.
- [48] A. Barreto, L. Pralon, B. Pompeo, M. Pralon, and G. Beltrao, “FPGA design and implementation of a real-time FM/PM pseudo random waveform generation for noise radars,” in *2020 IEEE Radar Conference (RadarConf20)*, 2020, pp. 1–6.
- [49] G. Galati, G. Pavan, K. Savci, and C. Wasserzier, “Noise radar technology: Waveforms design and field trials,” *Sensors*, vol. 21, 2021.
- [50] C. Wasserzier, “Exploiting the low Doppler tolerance of noise radar to perform precise velocity measurements on a short set of data,” *Signals*, vol. 2, pp. 25–40, 2021.
- [51] E. Kim, I.-k. Kim, S. Han, J. Lee, and S.-j. Shin, “A wideband noise radar system using a phased array with true time delay,” *Remote Sensing*, vol. 14, 2022.
- [52] D. K. Barton, *Modern Radar System Analysis*. Artech House, 1988.

- [53] M. I. Skolnik, *Radar handbook*, 3rd ed. McGraw-Hill Education, 2008.
- [54] X. Xu and R. M. Narayanan, “Range sidelobe suppression technique for coherent ultra wide-band random noise radar imaging,” *IEEE Transactions on Antennas and Propagation*, vol. 49, pp. 1836–1842, 2001.
- [55] A. Nelander, “Inverse filtering for noise radar processing,” in *2006 International Radar Symposium*, 2006, pp. 1–4.
- [56] F. Colone, R. Cardinali, and P. Lombardo, “Cancellation of clutter and multipath in passive radar using a sequential approach,” in *2006 IEEE Conference on Radar*, 2006, pp. 1–7.
- [57] S. R. J. Axelsson, “Random noise radar/sodar with ultrawideband waveforms,” *IEEE Transactions on Geoscience and Remote Sensing*, vol. 45, pp. 1099–1114, 2007.
- [58] K. Kulpa, “The CLEAN type algorithms for radar signal processing,” in *2008 Microwaves, Radar and Remote Sensing Symposium*, 2008, pp. 152–157.
- [59] F. Colone, D. W. O’Hagan, P. Lombardo, and C. J. Baker, “A multistage processing algorithm for disturbance removal and target detection in passive bistatic radar,” *IEEE Transactions on aerospace and electronic systems*, vol. 45, pp. 698–722, 2009.
- [60] J. L. Garry, C. J. Baker, and G. E. Smith, “Evaluation of direct signal suppression for passive radar,” *IEEE Transactions on Geoscience and Remote Sensing*, vol. 55, pp. 3786–3799, 2017.
- [61] C. Wasserzier, P. Wojaczek, D. Cristallini, J. Worms, and D. O’Hagan, “Doppler-spread clutter suppression in single-channel noise radar,” in *2019 International Radar Conference (RADAR)*, 2019, pp. 1–4.
- [62] P. Wojaczek, F. Colone, D. Cristallini, and P. Lombardo, “Reciprocal-filter-based stap for passive radar on moving platforms,” *IEEE Transactions on Aerospace and Electronic Systems*, vol. 55, pp. 967–988, 2019.
- [63] G. Paolo Blasone, F. Colone, P. Lombardo, P. Wojaczek, and D. Cristallini, “Passive radar DPCA schemes with adaptive channel calibration,” *IEEE Transactions on Aerospace and Electronic Systems*, vol. 56, pp. 4014–4034, 2020.
- [64] J. S. Kulpa, L. u. Maślikowski, and M. Malanowski, “Filter-based design of noise radar waveform with reduced sidelobes,” *IEEE Transactions on Aerospace and Electronic Systems*, vol. 53, pp. 816–825, 2017.
- [65] K. Savci, G. Galati, and G. Pavan, “Low-PAPR waveforms with shaped spectrum for enhanced low probability of intercept noise radars,” *Remote Sensing*, vol. 13, 2021.
- [66] G. Galati, G. Pavan, and C. Wasserzier, “Signal design and processing for noise radar,” *EURASIP Journal on Advances in Signal Processing*, vol. 2022, 2022.

- [67] S. Lloyd, “Enhanced sensitivity of photodetection via quantum illumination,” *Science*, vol. 321, pp. 1463–1465, 2008.
- [68] S.-H. Tan, B. I. Erkmen, V. Giovannetti, S. Guha, S. Lloyd, L. Maccone, S. Pirandola, and J. H. Shapiro, “Quantum illumination with Gaussian states,” *Phys. Rev. Lett.*, vol. 101, p. 253601, 2008.
- [69] J. H. Shapiro, “The quantum illumination story,” *IEEE Aerospace and Electronic Systems Magazine*, vol. 35, pp. 8–20, 2020.
- [70] F. Daum, “A system engineering perspective on quantum radar,” in *2020 IEEE International Radar Conference (RADAR)*, 2020, pp. 958–963.
- [71] R. Jonsson, “Quantum and classical metrology for noise radar,” PhD dissertation, Chalmers University of Technology, Göteborg, Sweden, October 2024.
- [72] D. W. O’Hagan, C. J. Baker, and H. D. Griffiths, “Passive coherent location (PCL) radar demonstrator,” in *Bistatic-Multistatic Radar and Sonar Systems. In Proceedings of the meeting RTO-MP-SET-095, RTO, Neuilly-sur-Seine, France*, vol. 20, 2007.
- [73] H. Kuschel and D. O’Hagan, “Passive radar from history to future,” in *11-th INTERNATIONAL RADAR SYMPOSIUM*, 2010, pp. 1–4.
- [74] C. R. Berger, B. Demissie, J. Heckenbach, P. Willett, and S. Zhou, “Signal processing for passive radar using OFDM waveforms,” *IEEE Journal of Selected Topics in Signal Processing*, vol. 4, pp. 226–238, 2010.
- [75] M. Malanowski and K. Kulpa, “Two methods for target localization in multi-static passive radar,” *IEEE transactions on Aerospace and Electronic Systems*, vol. 48, pp. 572–580, 2012.
- [76] J. E. Palmer, H. A. Harms, S. J. Searle, and L. Davis, “DVB-T passive radar signal processing,” *IEEE Transactions on Signal Processing*, vol. 61, pp. 2116–2126, 2013.
- [77] H. Kuschel, D. Cristallini, and K. E. Olsen, “Tutorial: Passive radar tutorial,” *IEEE Aerospace and Electronic Systems Magazine*, vol. 34, pp. 2–19, 2019.
- [78] H. D. Griffiths and C. J. Baker, *An introduction to passive radar*. Artech House, 2022.
- [79] D. W. O’Hagan and C. J. Baker, “Passive bistatic radar (PBR) using FM radio illuminators of opportunity,” in *2008 New Trends for Environmental Monitoring Using Passive Systems*, 2008, pp. 1–6.
- [80] P. Samczyński, K. Abratkiewicz, M. Płotka, T. P. Zieliński, J. Wszołek, S. Hausman, P. Korbel, and A. Ksieżyk, “5G network-based passive radar,” *IEEE Transactions on Geoscience and Remote Sensing*, vol. 60, pp. 1–9, 2022.
- [81] K. Jedrzejewski, K. Kulpa, M. Malanowski, and M. Pożoga, “Experimental trials of space object detection using LOFAR radio telescope as a receiver in passive radar,” in *2022 IEEE Radar Conference (RadarConf22)*, 2022, pp. 1–6.

- [82] M. Malanowski, M. Baczyk, M. Plotka, K. Jedrzejewski, M. Bartoszewski, G. Krawczyk, and M. Zywek, "MATLAB-based multistatic passive radar demonstrator," in *2023 IEEE International Radar Conference (RADAR)*, 2023, pp. 1–6.
- [83] M. Ankel, "Google Drive: Bistatic Measurment Results," https://drive.google.com/drive/folders/1A4fM1DPaR9BoZX4P-dx3t2ZBoQtX_2kp?usp=sharing.
- [84] N. J. Willis, *Bistatic Radar*, 2nd ed. SciTech Publishing, 2005.
- [85] <https://freepngimg.com/png/23765-jet-image>.
- [86] S. M. Kay, *Fundamentals of Statistical Signal Processing, Volume II - Detection Theory*. Prentice Hall PTR, 1998.
- [87] Saab Internal Documentation.
- [88] N. J. Willis and H. D. Griffiths, Eds., *Advances in Bistatic Radar*. SciTech Publishing, Inc., 2007.
- [89] J. G. Proakis and M. Salehi, *Digital communications*, 5th ed. McGraw-hill New York, 2007.
- [90] The MathWorks Inc. , *PN Sequence Generator*, Natick, Massachusetts, United States, Accessed: August 14, 2023.
- [91] Response from reviewer in the submission process of "Bistatic Noise Radar: Demonstration of Correlation Noise Suppression".
- [92] F. Harris, "On the use of windows for harmonic analysis with the discrete Fourier transform," *Proceedings of the IEEE*, vol. 66, pp. 51–83, 1978.
- [93] A. Papoulis and S. Pillai, *Probability, Random Variables, and Stochastic Processes*, 4th ed. McGraw-Hill, 2002.
- [94] S. R. J. Axelsson, "On the theory of noise Doppler radar," in *IGARSS 2000. IEEE 2000 International Geoscience and Remote Sensing Symposium. Taking the Pulse of the Planet: The Role of Remote Sensing in Managing the Environment. Proceedings (Cat. No.00CH37120)*, 2000, pp. 856–860.
- [95] J. W. Cooley and J. W. Tukey, "An algorithm for the machine calculation of complex Fourier series," *Mathematics of Computation*, vol. 19, pp. 297–301, 1965.
- [96] G. Galati, G. Pavan, and C. Wasserzier, "Optimal processing in noise radar: Implementation problems," in *2019 Signal Processing Symposium (SPSympo)*, 2019, pp. 45–50.
- [97] T. L. Marzetta, E. A. Martinsen, and C. P. Plum, "Fast pulse Doppler radar processing accounting for range bin migration," in *The Record of the 1993 IEEE National Radar Conference*, 1993, pp. 264–268.

- [98] Y. Li, T. Zeng, T. Long, and Z. Wang, “Range migration compensation and doppler ambiguity resolution by keystone transform,” in *2006 CIE International Conference on Radar*, 2006, pp. 1–4.
- [99] R. P. Perry, R. C. DiPietro, and R. L. Fante, “Coherent integration with range migration using keystone formatting,” in *2007 IEEE Radar Conference*, 2007, pp. 863–868.
- [100] M. A. Richards, “The keystone transformation for correcting range migration in range-doppler processing,” *pulse*, vol. 1000, 2014.
- [101] K. M. Scott, W. C. Barott, and B. Himed, “The keystone transform: Practical limits and extension to second order corrections,” in *2015 IEEE Radar Conference (RadarCon)*, 2015, pp. 1264–1269.
- [102] J. Högbom, “Aperture synthesis with a non-regular distribution of interferometer baselines,” *Astronomy and Astrophysics Supplement*, vol. 15, pp. 417–426, 1974.
- [103] R. D. Fry and D. A. Gray, “CLEAN deconvolution for sidelobe suppression in random noise radar,” in *2008 International Conference on Radar*, 2008, pp. 209–212.
- [104] X. Bai, J. Han, J. Zhao, Y. Feng, and R. Tao, “Clutter cancellation in passive radar using batch-based CLEAN technique,” *EURASIP Journal on Advances in Signal Processing*, vol. 63, pp. 1–19, 2021.
- [105] K. S. Kulpa, “Simple sea clutter canceller for noise radar,” in *2006 International Radar Symposium*, 2006, pp. 1–4.
- [106] P. Stoica and R. L. Moses, *Spectral analysis of signals*. Pearson Prentice Hall Upper Saddle River, NJ, 2005, vol. 452.
- [107] M. Zatman, “How narrow is narrowband?” *IEE Proceedings-Radar, Sonar and Navigation*, vol. 145, pp. 85–91, 1998.
- [108] <https://wirelesspi.com/fractional-delay-filters-using-the-farrow-structure/>.
- [109] Intermodulation Products AB, *Intermodulation Products – Vivace*, Segersta, Sweden, Accessed: May 17, 2023.
- [110] National Instruments, Manual, July 07, 2024. Accessed: February 11, 2020. [Online], Available: <https://www.ni.com/docs/en-US/bundle/pxie-5170-specs/page/specs.html> , “PXIE-5170 specifications.”
- [111] Analog Devices, User Guide, August 03, 2021. Accessed: January 18, 2022. [Online], Available: <https://wiki.analog.com/resources/eval/ads7-v2>, “ADS7-V2EBZ HIGH SPEED EVALUATION BOARD.”
- [112] Analog Devices, User Guide UG-1526, rev 0, November, 2019. Accessed: January 18, 2022. [Online], Available: <https://www.analog.com/media/en/technical-documentation/user-guides/AD9161-9162-9163-9164-UG-1526.pdf>, “AD9161/AD9162/AD9163/AD9164 User Guide.”

- [113] Mini-Circuits , *High Power Amplifier ZVE-2W-272X+*, Brooklyn, New York, United States, Accessed: May 22, 2021.
- [114] ———, *Bandpass Filter ZX75BP-1307-S+*, Brooklyn, New York, United States, Accessed: May 22, 2021.
- [115] Spectratime, Manual, rev 2.10, June 19, 2017. Accessed: January 18, 2022. [Online], Available: <https://www.orolia.com/product/gxclok-500-gps-gnss-ocxo-clock-module/>, “iSync+ Smart GXClok-500 Manual.”
- [116] Qorvo Us, Inc. , *QPD1006 Data Sheet Rev. C*, Greensboro, North Carolina, United States, Accessed: June 20, 2023.
- [117] Ampleon, Application note, rev 2, September 1, 2015. Accessed: January 18, 2020. [Online], Available: <https://www.ampleon.com/>, “Bias module for 50 V GaN demonstration boards.”
- [118] N. Tervo, B. Khan, O. Kursu, J. P. Aikio, M. Jokinen, M. Leinonen, M. Juntti, T. Rahkonen, and A. Pärssinen, “Digital predistortion of phased-array transmitter with shared feedback and far-field calibration,” *IEEE Transactions on Microwave Theory and Techniques*, vol. 69, pp. 1000–1015, 2021.
- [119] Xilinx, Inc. , *ZCU111 Evaluation Board User Guide (UG1271) v1.4* , San Jose, California, United States, Accessed: May 17, 2023.
- [120] M. Tholén, “Digital measurement and control of microwave quantum circuits,” PhD dissertation, KTH Royal Institute of Technology, Stockholm, Sweden, January 2024.
- [121] Xilinx, Inc. , *RF Data Converter Interface User Guide (UG1309) v1.4* , San Jose, California, United States, Accessed: Jan 11, 2024.
- [122] O. L. Frost, “An algorithm for linearly constrained adaptive array processing,” *Proceedings of the IEEE*, vol. 60, pp. 926–935, 1972.
- [123] T. Wild, V. Braun, and H. Viswanathan, “Joint design of communication and sensing for beyond 5G and 6G systems,” *IEEE Access*, vol. 9, pp. 30 845–30 857, 2021.
- [124] J. A. Zhang, M. L. Rahman, K. Wu, X. Huang, Y. J. Guo, S. Chen, and J. Yuan, “Enabling joint communication and radar sensing in mobile networks—a survey,” *IEEE Communications Surveys & Tutorials*, vol. 24, pp. 306–345, 2022.
- [125] G. Callebaut, L. Liu, T. Eriksson, L. Van der Perre, O. Edfors, and C. Fager, “6G radio testbeds: Requirements, trends, and approaches,” *IEEE Microwave Magazine*, vol. 25, pp. 14–31, 2024.
- [126] C. Fager, T. Eriksson, F. Barradas, K. Hausmair, T. Cunha, and J. C. Pedro, “Linearity and efficiency in 5G transmitters: New techniques for analyzing efficiency, linearity, and linearization in a 5G active antenna transmitter context,” *IEEE Microwave Magazine*, vol. 20, pp. 35–49, 2019.